

# Full 5D characterisation of the Sagittarius stream with *Gaia* DR2 RR Lyrae

P. Ramos<sup>1,\*</sup>, C. Mateu<sup>2</sup>, T. Antoja<sup>1</sup>, A. Helmi<sup>3</sup>, A. Castro-Ginard<sup>1</sup>, and E. Balbinot<sup>3</sup>

<sup>1</sup> Dept. FQA, Institut de Ciències del Cosmos (ICCUB), Universitat de Barcelona (IEEC-UB), Martí Franquès 1, E-08028 Barcelona, Spain

<sup>2</sup> Departamento de Astronomía, Instituto de Física, Universidad de la República, Iguá 4225, CP 11400 Montevideo, Uruguay

<sup>3</sup> Kapteyn Astronomical Institute, University of Groningen, Landleven 12, 9747 AD Groningen, The Netherlands

Received XXXX; accepted XXXX

## ABSTRACT

**Context.** The Sagittarius stream is one of the best tools that we currently have to estimate the mass and shape of our Galaxy. However, assigning membership and obtaining the phase-space distribution of the stars that form the tails is quite challenging.

**Aims.** Our goal is to produce a catalogue of RR Lyrae stars of Sagittarius and obtain an empiric measurement of the trends along the stream in sky position, distance and tangential velocities.

**Methods.** We generate two initial samples from the *Gaia* DR2 RR Lyrae catalogue: one, selecting only the stars within  $\pm 20^\circ$  of the orbital plane of Sagittarius (Strip) and the other, the result of applying the Pole Count Map (nGC3) algorithm. We then use the model-independent, deterministic method developed in this work to remove most of the contamination by detecting and isolating the stream in distance and proper motions.

**Results.** The output is two empiric catalogues: the Strip sample (higher-completeness, lower-purity) which contains 11 677 stars, and the nGC3 sample (higher-purity, lower-completeness) with 6 608 stars. We characterise the changes along the stream in all the available dimensions, the 5 astrometric ones plus the metallicity, covering more than  $2\pi$  rad in the sky and obtain new estimates for the apocentres and the mean [Fe/H] of the RR Lyrae population. Also, we show the first map of the two components of the tangential velocity, thanks to the combination of distances and proper motions. Finally, we detect the bifurcation in the leading arm and report no significant difference between the two branches, either in metallicity, kinematics or distance.

**Conclusions.** We provide the largest sample of RR Lyrae candidates of Sagittarius, which can be used as an input for a spectroscopic follow-up or as a reference for the new generation of models of the stream through the interpolators in distance and velocity that we have constructed.

**Key words.** Galaxy: halo – Stars: variables: RR Lyrae – Galaxies: dwarf – astrometry

## 1. Introduction

The Sagittarius (Sgr) dwarf galaxy (Ibata et al. 1994) is the first detected and most conspicuous relic of an accretion and tidal destruction event in our Galaxy. Since its discovery (Mateo et al. 1996; Totten & Irwin 1998), the stream has been studied extensively using different tracers and techniques, trying to map its full extent and various wraps around the Galaxy which, combined with kinematic information, can be used to understand the dynamics of its tidal disruption and to infer properties of the Galactic dark matter halo (Law & Majewski 2010; Deg & Widrow 2013; Fardal et al. 2019).

Compared to simpler and thinner streams, e.g. GD-1, Pal 5 or Orphan, among dozens now known in our Galaxy (see Grillmair & Carlin 2016; Mateu et al. 2018; Shipp et al. 2018; Ibata et al. 2019), the Sgr stream has several main characteristics that make it as interesting, as they make it challenging to observe and to model. The stream is luminous and abundantly populated with stars, it is roughly planar, wraps around the Galaxy at least twice (Martínez-Delgado et al. 2004), and its (observed) debris spans distances from 20 to over 100 kpc (Sesar et al. 2017a). The extended star formation history (de Boer et al. 2015) of its luminous and massive progenitor has produced complex stellar

population and metallicity gradients along the stream and, because the debris is all around the sky and spans such a large distance range, it is observationally demanding to trace in a continuous manner. Despite having a high surface brightness and a stellar population clearly different from that of the halo, which should in principle facilitate its detection, we still lack a model that can convincingly reproduce the stream. The long-standing problem being the lack of kinematic data and the reproducibility of features such as the tail's bifurcations or the angular separation between apocentres (Belokurov et al. 2006; Koposov et al. 2012; Navarrete et al. 2017; Belokurov et al. 2014; Gibbons et al. 2016).

One of the key elements to properly model the in-fall of Sgr is to characterise the spatial distribution and kinematics of its different populations throughout the sky, in a continuous and homogeneous way. Majewski et al. (2003) made the first all-sky map of the tails using 2MASS M-giants, followed by many later studies that obtained radial velocities for red giants, blue horizontal branch stars and other tracers, usually in small patches along the stream (e.g. Li et al. 2019, and references in Belokurov et al. 2014). Recently, Antoja et al. (2020), hereafter A20, used the precise astrometry of the *Gaia* second data release (DR2; *Gaia* Collaboration et al. 2018) to detect the Sgr stream from proper motion alone without having to select an specific stellar

\* email: pramos@fqa.ub.edu

type, and determine for the first time its proper motion along the path of the full stream. However, they did not obtain distance estimates since the parallaxes at such faint magnitudes provide little information and would require a thorough study of the astrometric systematics (global and local). In any case, this would only allow distance estimates out to a few tens of kpc. Tracers for which photometric distances can be obtained are thus better to study the stream to its full extent in a comprehensive way.

Before the publication of *Gaia* DR2, Hernitschek et al. (2017) used PanSTARRS-1 (PS1; Chambers et al. 2016) RR Lyrae stars to measure distances to the Sgr tails and were able to trace the Sgr leading and trailing arms all around the sky, while characterising its distance and line-of-sight depth. Later, Sesar et al. (2017a) identified new Sgr features at distances over 100 kpc using the same sample. The advantage of using RR Lyrae stars is that they are excellent as standard candles, their photometric distance errors being  $\sim 7\%$  in the optical (Mateu et al. 2012) or as good as  $\sim 3\%$  in the infrared (Sesar et al. 2017b) even without prior knowledge of their metallicity. This is an order of magnitude more precise than the  $\sim 20 - 30\%$  errors that can be achieved with K and M giants (Liu et al. 2014), as these are far more sensitive to metallicity. This has made them, the RR Lyrae, a standard in studies of the halo structure (for a review see Table 4 in Mateu & Vivas 2018) and substructure, serving to identify new streams and overdensities (Vivas et al. 2001; Duffau et al. 2006; Sesar et al. 2010; Mateu et al. 2018); to extend and find the connection between seemingly different substructures, like the Orphan and Chenab streams (Koposov et al. 2019); and, combined with *Gaia* DR2 kinematics, to provide a comprehensive 5D view of the Orphan (Koposov et al. 2019) and Pal 5 streams (Price-Whelan et al. 2019). RR Lyrae, being old ( $\geq 10$  Gyr) and metal-poor ( $[\text{Fe}/\text{H}] \lesssim -0.5$ ) stars (Catalan & Smith 2015), are expected to dominate the outskirts of dwarf galaxies (Koleva et al. 2011, and references therein) and are therefore the first to be stripped, tracing the ancient components of a stream and thus contributing to the dynamically oldest wraps.

An all-sky view of the kinematics of the Sgr stream with RR Lyrae is still limited, though, because radial velocities are observationally demanding to obtain due to the stars' pulsations. Currently, these are only available for a few dozen RR Lyrae in selected fields along the Sgr stream (Vivas et al. 2005). In this work, we aim to provide a cohesive 5-D view of the distance and proper motions of the Sgr stream using RR Lyrae stars. In Section 2 we describe the input catalogue — the RR Lyrae identified as such by the *Gaia* variability pipelines complemented with the PS1 catalogue. In Section 3 we derive distances for these RR Lyrae stars and describe our selection method based on sky coordinates, proper motions and distances, and use no prior information. In Section 4 we present our results providing an entirely empirical characterisation of the stream including e.g. its proper motion, galactocentric distance, tangential velocities, and the bifurcation. Finally, we present our conclusions in Section 5.

## 2. RR Lyrae and *Gaia* sample

The second data release (Gaia Collaboration et al. 2018) of the *Gaia* mission (Gaia Collaboration et al. 2016) has provided not only positions, magnitudes and proper motions for more than a billion stars, but also a vast catalogue of variable sources (Holl et al. 2018). For a detailed description of the detection, classification and post-processing pipelines we refer the reader also to Eyer et al. (2017) and Rimoldini et al. (2019). Among those detected variable sources, there are 140 784 RR Lyrae that have at

**Table 1.** Number of stars in each sample at each step of the selection process.

Stage	nGC3	Strip
Initial sample	13 004	76 872
Distance selection	7 953	18 045
$\mu_{\alpha^*}$ selection	6 797	12 583
$\mu_{\delta}$ selection	6 608	11 677

least 12 good *G*-band transits which have been validated by the Specific Objects Study (SOS) pipeline (Clementini et al. 2019). We have further increased the number to 228 904 sources by including those classified as RR Lyrae by Holl et al. (2018) and Rimoldini et al. (2019), but not processed by SOS due to the small number of observations available in DR2. We then apply the filter recommended in Rimoldini et al. (2019) to remove obvious contaminants: `phot_bp_rp_excess_factor > 2 OR NULL`, leaving 175 164 RR Lyrae. Finally, we include 11 318 stars identified as *bona fide* RR Lyrae in the PanSTARRS1 catalogue (Sesar et al. 2017b), but not classified as such by the *Gaia* pipelines. We identify these stars in the DR2 `gaia_source` table by cross-matching their positions on the sky with a  $1''$  tolerance, and retrieve their astrometric data.

After removing the stars with no proper motions we obtain a list of 182 495 stars, 122 745 of which have been processed by the SOS pipeline. For some of them, the SOS team has derived photometric metallicities and absorption in the *G* band. In particular, 39 129 of them have both quantities simultaneously, which we use in Sect. 3.2 to obtain a first measurement of the metallicity distribution along the stream. As stated in Holl et al. (2018), the *Gaia* catalogue of variable sources is not meant to be complete and, in fact, we do not expect the completeness to be above 80% when taking only sources with more than 12 Field of View (FoV) transits (see also Mateu et al., in prep.).

## 3. Selection of RR Lyrae in the Sagittarius stream

Our aim is to detect the Sgr stream's RR Lyrae from scratch to produce a characterisation as empirical as possible. To do so, we select from the list of stars with proper motions presented in the previous section two sets of initial candidates: the Strip and the nGC3 selections (Sect. 3.1), later pruned to filter out contaminants based on distance (Sect. 3.3) and kinematic information (Sect. 3.4 and 3.5). We use these two different selections since they offer different advantages as we shall see below. In Table 1 we show the number of stars remaining after each selection step.

### 3.1. Initial selections: Strip and nGC3

**Strip selection.** A high-completeness, low-purity sample: A first straightforward list of candidates can be obtained by selecting stars within  $20^\circ$  of the orbital plane defined by the pole  $(l,b)=(273^\circ.8; 13^\circ.5)$  from Majewski et al. (2003). This is exactly equivalent to selecting stars with  $|\tilde{B}_\odot| < 20^\circ$  in the Sgr coordinate frame<sup>1</sup>, a spherical heliocentric frame rotated to have the stream's plane at  $\tilde{B}_\odot = 0^\circ$  and the Sgr dwarf remnant at  $\tilde{L}_\odot = 0^\circ$ . The resulting selection contains 76 872 RR Lyrae (41% of the full catalogue).

This selection is expected to be highly complete, limited only by the completeness of the input catalogue itself, as no

<sup>1</sup> In this work, we use the convention by Belokurov et al. (2014).

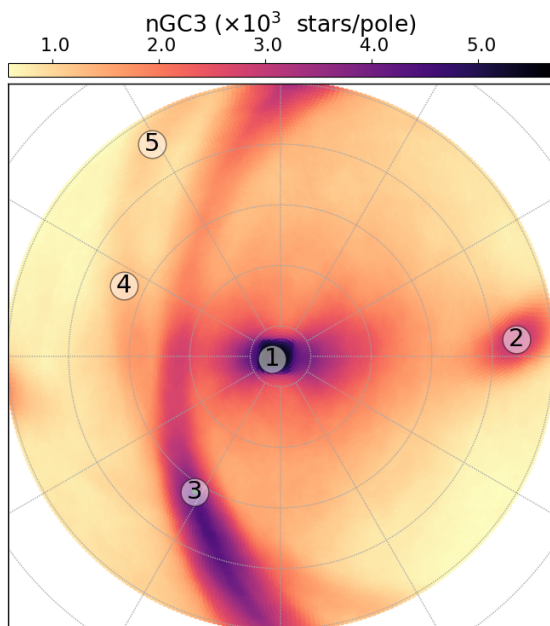


**Fig. 1.** Pole Count Map of the RR Lyrae catalogue described in Sect. 2. The Galactic disc produces the large concentration at (1), while the peaks (3),(4) and (5) are related to the Large and Small Magellanic clouds. The prominent signal on the right, (2), is caused by the Sgr stream.

kinematic nor any additional information (e.g. metallicity) is required. However, precisely because no information other than sky position is used, a large fraction of contaminants is expected, mostly due to the thick disc and halo. This contamination will be reduced significantly after the next selection steps.

**nGC3 selection.** A low-completeness, high-purity sample: Great circle cell counts methods, grouped in the xGC3 family (Johnston et al. 1996; Mateu et al. 2011, 2017), are aimed at the detection of groups of stars that populate an orbital plane different from that of the Milky Way disc. In its most basic implementation, this approach relies on the fact that the stars in a stream lie approximately on a plane through the Galactic potential’s centre of symmetry. Geometrically, this implies that the stream is confined to a great circle uniquely defined by the normal vector (pole) of the orbital plane. Therefore, if we grid the sky<sup>2</sup> and, for each cell, count the number of stars in a wafer of a certain width perpendicular to it, we should detect an overdensity whenever we align said wafer with the orbital plane of a stream. The result is a pole count map (PCM), which is a density map of the number of stars associated to each pole and, hence, great circle.

The nGC3 method, introduced in Abedi et al. (2014), requires also proper motion information in the pole counting. In this method the stars’ velocities are required to lie in the same great circle as their positions, within a certain tolerance. This helps prune out contaminant stars that lie in a given great circle band by chance. We cannot take this approach in the heliocentric frame, because then the peculiar velocity of the Sun would dominate the PCM. Instead, the nGC3 pole counts are made in

<sup>2</sup> For streams that are too close to the Sun, projecting their orbit onto the Celestial sphere might introduce projection effects, i.e. the Galactic parallax becomes non-negligible.

the galactocentric reference frame, for which we assume a distance from the Sun to the Galactic Center (GC) of  $R_{\odot}=8.0$  kpc (Camarillo et al. 2018), a velocity of the Sun with respect to the Local Standard of Rest (LSR)  $[U_{\odot}, V_{\odot}, W_{\odot}] = [11.10, 12.24, 7.25]$  km s<sup>-1</sup> (Schönrich et al. 2010) and  $V_{LSR} = 240$  km s<sup>-1</sup> (Reid et al. 2014). Obviously, we also require a distance to each star which implies assuming a metallicity (see Sect. 3.2). We chose as a first value  $[\text{Fe}/\text{H}] = -1.7$  dex. We find that the PCM does not change significantly within the range of metallicities typical for RR Lyrae in the halo:  $-1.5 \text{ dex} \leq [\text{Fe}/\text{H}] \leq -1.7$  dex.

Figure 1 shows the resulting PCM for the RR Lyrae, using a tolerance of 5° for both positional and velocity vectors. The method also returns a list of peaks, i.e. local maxima, ordered by the number of counts contained within the corresponding pole. As expected, we observe a peak (label 1) at the centre caused by the disc. The second most dominant peak (label 2) is that produced by the Sgr stream. We also see signatures produced by the Large (label 3) and Small (labels 4 and 5) Magellanic clouds which, being concentrated on the sky, make trails instead of compact overdensities.

The nGC3 selection is made by extracting the RR Lyrae stars associated to the cells, or poles, around peak 2 within the 25-percentile of the maximum counts in that peak. This results in a preliminary list of candidates of 13 004 (7% of the full RR Lyrae catalogue). This sample is expected to be of lower completeness than the Strip selection because the method can introduce correlations between the spatial position and the proper motions and, more importantly, a dependence on the observational errors which can translate into kinematical biases. In particular, the method by construction selects against stars with significant motions perpendicular to the stream’s plane, making it unsuitable to study aspects such as velocity dispersion profiles, as we shall discuss later in Sec. 4.6. By contrast, the nGC3 sample is expected to be of higher purity, hence, better suited for purposes such as the selection of targets for spectroscopic follow-up.

Having a first list of candidates, we next look for trends in distances and proper motions to refine our selection. Only for the rest of this section, to avoid repetition, we use the nGC3 sample to show how our selection methodology works. This sample, by construction, is less contaminated than the Strip sample and allows us to illustrate more clearly the way we separate the candidate stars from the contamination. Wherever important differences with the Strip sample arise they will be discussed in the text. The plots corresponding to the Strip selection can be found in Appendix C.

### 3.2. Distance determination

To determine the distances we begin by using the linear relation for the *Gaia* *G* band given in Muraveva et al. (2018):

$$M_G = 0.32_{-0.04}^{+0.04} [\text{Fe}/\text{H}] + 1.11_{-0.06}^{+0.06}. \quad (1)$$

This relation returns the absolute magnitude of the RR Lyrae star, given its metallicity in the Zinn & West (1984) scale (hereafter, ZW84). We note, however, that the metallicity given by DPAC is calculated from the Fourier parameters of the light curve (Clementini et al. 2019). In particular, in the case of RR Lyrae of type RRab, the metallicity is calibrated with the prescription of Nemeč et al. (2013) which, for the range of Periods and Fourier parameters of our sample (c.f. their Fig. 12), closely matches the Jurcsik & Kovacs (1996) metallicity scale. As noted in Gratton et al. (2004) and Di Fabrizio et al. (2005), there is a

systematic difference of +0.3 dex between the metallicities derived from photometry in the Jurcsik & Kovacs (1996) scale and those calculated with spectroscopy<sup>3</sup>. Therefore, for our particular case, we subtract 0.3 dex to each RRab to put the metallicities from DPAC in the ZW84 scale. This is not the case for the stars of type RRc, since their metallicity is given in a scale already similar enough to ZW84 (Nemec et al. 2013; Clementini et al. 2019).

Even though we have a way to compute the absolute magnitude for our stars, the metallicity is only available for a small fraction of them ( $\sim 35\%$ , see Clementini et al. 2019). Additionally, the Sgr stream presents a gradient in metallicity (e.g., Zhang et al. 2017; Hayes et al. 2019). Our approach is to test first whether there is a metallicity gradient for the RR Lyrae stars with measured metallicity. This is important since it could introduce a distance bias along  $\tilde{\Lambda}_\odot$ . However, we will find that there is not (see below), and we will assign an average metallicity to the rest of RR Lyrae.

To calculate the distances we use the well known relation for the apparent magnitude of a star,

$$d [pc] = 10^{(m_G - M_G - A_G)/5 + 1}, \quad (2)$$

for all stars with reported metallicity and absorption in the nGC3 sample. In particular, we choose a sample of 884 stars between 20 kpc and 50 kpc from the Sun, i.e. preferentially selecting stars belonging to the stream (c.f. Fig. 4 of Hernitschek et al. 2017), all of which happen to be RRab according to the classification by SOS.

In Fig. 2 we study the dependence of the metallicity on  $\tilde{\Lambda}_\odot$ . The gradient we measure is, respectively for the leading and the trailing arms,  $(-1.5 \pm 0.4) \times 10^{-3} \text{ dex deg}^{-1}$  and  $(0.9 \pm 3.7) \times 10^{-4} \text{ dex deg}^{-1}$ . While the latter is clearly compatible with zero, the former shows some sign of a gradient. Still, this gradient can be heavily influenced by the contamination, and the variations in metallicity that this would imply ( $0.15 \text{ dex every } 100^\circ$ ) are smaller than the typical photometric metallicity precision ( $\sim 0.2 \text{ dex}$ ). Therefore, we recover a mean metallicity  $[\text{Fe}/\text{H}]_{\text{ZW}} = -1.61 \text{ dex}$  with no trace of a gradient, in good agreement with previous studies of the RR Lyrae population of Sgr (Cseresnjés 2001). As for the statistical uncertainty on the mean, we find  $\frac{\sigma_{[\text{Fe}/\text{H}]}}{\sqrt{N}} = 0.02 \text{ dex}$ . After repeating the measurement for the Strip sample, we obtain the same result but with a smaller uncertainty ( $\frac{\sigma_{[\text{Fe}/\text{H}]}}{\sqrt{N}} = 0.01 \text{ dex}$ ). We re-visit this determination in Sect. 4.4, after having selected a reliable sample of Sgr stars, and we obtain the same value within the uncertainties.

Given that there is no significant gradient, we impose the mean metallicity on all the candidate stars. We note that the distribution of apparent magnitude of the RR Lyrae type C is for all purposes the same as that of the RRab. Assuming that there is no segregation between both types inside the stream, their distance distribution at any given  $\tilde{\Lambda}_\odot$  should then be the same. Therefore, we can use the same metallicity for both as long as we apply the same calibration, i.e. Eq. 1.

In addition, to obtain a distance estimation for each star we need the absorption in the *G* band. For that, we use the Schlegel et al. (1998) dust maps with the Schlafly & Finkbeiner (2011) recalibration and the relations that allows us to translate reddening to absorption (Appendix A). Having done that, we apply Eq. 1

<sup>3</sup> The offset was calculated with respect to the Harris (1996) spectroscopic scale which has almost no shift compared to the ZW84 scale used in this work (Gratton et al. 2004).

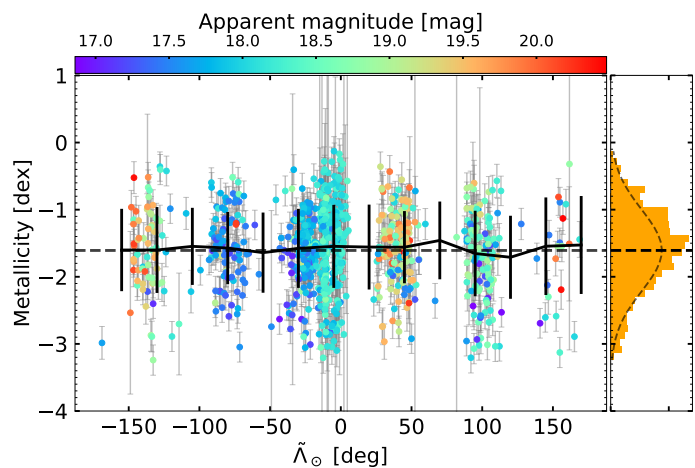


**Fig. 2.** Metallicity dependence on  $\tilde{\Lambda}_\odot$  for the stars selected by the nGC3 method that have a measured metallicity and absorption. Only those stars between 20 kpc and 50 kpc are shown (884 RRab), coloured by their apparent magnitude. The dashed line corresponds to the mean metallicity (-1.61 dex) whereas the solid line is the running median and 1 sigma interval within bins of  $50^\circ$  every  $25^\circ$ . On the right, we include the metallicity distribution and a Gaussian fit to the data:  $\mu = -1.61 \text{ dex}$  and  $\sigma = 0.61 \text{ dex}$ .

and 2 to the whole list of candidates and propagate the uncertainties in metallicity, apparent magnitude, coefficients of Eq.1 and absorption<sup>4</sup> using the Jacobian of the transformation.

Apart from the statistical uncertainties, we also have a systematic source of uncertainty: our metallicity zero-point. We have subtracted 0.3 dex to the metallicities reported by SOS to obtain values in the ZW84 scale. Nevertheless, if that is not the right offset we would be biasing all distances by a fix proportion:

$$\frac{D(\Delta Z)}{D_0} = 10^{-\frac{0.32}{5} \Delta Z}, \quad (3)$$

where  $\Delta Z$  is the difference between the zero-point that we assume and the true one. For instance, having no zero-point in reality ( $\Delta Z = +0.3 \text{ dex}$ ) and having a zero-point double of what we assumed ( $\Delta Z = -0.3 \text{ dex}$ ), respectively, and for a distance of 25 kpc, we would obtain 23.92 kpc (-4.3%) and 26.13 kpc (+4.5%). We expect the true zero-point to be closer to our value and therefore the systematic error to be much smaller than 4%.

### 3.3. Distance selection

In the top panel of Fig. 3 we present the resulting distribution of distances with  $\tilde{\Lambda}_\odot$ . A conspicuous pattern emerges as a result of selecting sources belonging to the Sgr orbital plane. Nevertheless, there is still a noticeable fraction of contamination even after applying the nGC3 PCM technique: thick disc, halo and even the Sculptur dwarf Spheroidal at  $\tilde{\Lambda}_\odot \sim -75^\circ$  (the latter is easily removed). Continuing with the spirit of re-discovering the stream from scratch, we apply a method to select probable members that requires almost no assumptions and that we call Tailored Gaussian Mixture (hereafter, TGM).

The idea of the TGM is to select the pattern formed by the Sgr stars with  $\tilde{\Lambda}_\odot$  isolating it from the both the foreground and the background contamination. For a given bin of  $\tilde{\Lambda}_\odot$ , we process

<sup>4</sup> We find that, when propagating the errors in colours to the transformations from  $A_V$  to  $A_G$  by Monte Carlo sampling, the uncertainty in absorption can be taken to be 0.02 dex.

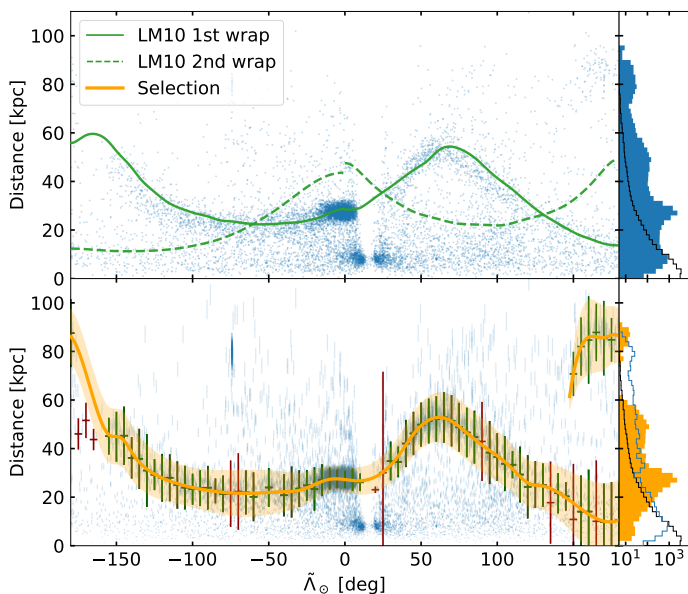


**Fig. 3.** Distance as a function of  $\tilde{\Lambda}_\odot$  for the stars in the Sgr stream. Top: all the candidates selected by the *nGC3* method. The green lines represent the predictions of the LM10 model for the first (solid) and second (dashed) wrap. The blue bars on the right are the histogram of the same stars, while the black steps correspond to the predictions from the mock catalogue (see text). Bottom: same stars, now with their associated uncertainties, adding green (red) error bars representing the parameters extracted from the good (bad) fit to the kernel associated with Sgr (see text). We also show in orange the interpolation of the centres (dashed line) and the two-sigma interval (shaded area). The histogram on the right shows now in orange the selected stars, in blue the remaining ones while the black one is the same as above.

the histogram of heliocentric distances and identify the different components (Sgr and contamination). Then, a Gaussian is fitted to each component to obtain their widths. The algorithm starts at the dwarf and uses it as an anchor since it is the dominant component at  $\tilde{\Lambda}_\odot = 0^\circ$ . The component corresponding to Sgr in the contiguous bins is assigned by finding the one with the highest continuity in heliocentric distance. When none of the components found are close enough to the one in the previous bin, we skip the bin and try with the next one. The details of the method can be found in Appendix B.

With this algorithm we obtain a deterministic measurement of the centre of the pattern as well as a first estimation of its depth. The result for the *nGC3* sample is shown in the bottom panel of Fig. 3 as error bars located at the centre of each bin in  $\tilde{\Lambda}_\odot$ . The error bars represent, vertically, the  $2\sigma$  interval of the dispersion recovered by the fit and horizontally, the size of the bin (barely visible). We note that using the same metallicity for all the stars actually increases the contamination because the foreground (thick disc) merges with the signal of the stream. Since the RR Lyrae in the thick disc tend to be more metal rich than those in Sgr, assigning an incorrectly smaller metallicity to these stars translates into larger distances and thus pushes its distribution towards that of the stream, hampering the separation. Finally, we detect by visual inspection that in some of the bins the Gaussian fit has not converged to a good solution. The two main causes are i) too few sources and ii) the components are too close to be resolved, resulting in an overestimated width. Those few cases (plotted in red in the bottom panel of Fig. 3) have been removed.

We finish by creating two splines with the good solutions (green error bars). The first, one that passes through the centres

and represents the change in the distance with  $\tilde{\Lambda}_\odot$  (orange line). We use the second one to trace the changes in depth of the stream and produce a smooth  $\sim 2\sigma$  confidence interval, as represented by the shaded orange area. We also show the smoothed median distance predicted by the Law & Majewski (2010) model (hereafter, LM10<sup>5</sup>). These solid (1st wrap) and dashed (2nd wrap) green lines can be seen to follow our orange track in some part of the stream. However, there are important differences which we comment on in Sect. 4. On the other hand, our results are in very good agreement with the recent determination of the pattern of Sgr obtained with RR Lyrae by Hernitschek et al. (2017) (see their Fig. 4).

The candidates are selected if they fall inside the orange shaded area, resulting in a set of 7 953 stars (61% of the initial *nGC3* sample). In the case of the Strip sample (Fig. C.1) the output of the TGM results in a selection of 18 045 stars (23%). Both samples contain field stars that require additional filters to be discarded, specially at  $\tilde{\Lambda}_\odot \geq 120^\circ$  where the Sgr stars get closer to the Sun and merge with the Virgo overdensity (Jurić et al. 2008). In that region we also have the presence of Sgr stars at a distance of  $\sim 90$  kpc, which correspond to the apocentre of the trailing arm.

We also include a comparison with a mock catalogue. We query the mock *Gaia* catalogue by Rybizki et al. (2018) in HEALPix bins of level 4 ( $\sim 14$  square degrees) along the orbital plane of Sgr selecting 2 000 stars for each patch in the sky. Then, we compute the true distances by simply inverting the true parallaxes and produce the heliocentric distance histograms shown in black on the right of Fig. 3 (normalised to the number of stars in the *nGC3* sample). The mock distribution presents a smooth exponential profile with no sign of bumps, in contrast with our data (blue filled histogram). With the mock as a reference, we gain an idea of the contamination that we expect at each portion of the stream, being the parts near pericentre the most susceptible. This corresponds to the beginning of the trailing tail and, especially, the far end of the leading one ( $\tilde{\Lambda}_\odot > 120^\circ$ ). After performing our selection (orange histogram at the bottom right panel of Fig. 3) we see that what we have discarded, i.e. what we consider contamination (blue line), resembles the mock distribution except for two details: i) at small distances, the effect mentioned earlier of using a wrong metallicity for the thick disc modifies the shape of the distribution and ii) the absolute value of counts at large distances is not the same. The later could be due either to a problem of normalisation between the thick disc and halo components of the mock or simply because the parameters of the model do not reproduce the observations accurately enough.

### 3.4. Proper motion selection: Right Ascension

We continue the selection of RR Lyrae candidates based now on their proper motion trends throughout the Sgr stream. In order to avoid overlap between the different wraps, we take those corresponding to the apocentre of the trailing arm and shift their location by  $-360^\circ$ . Therefore, from here on-wards the plots reach beyond  $-180^\circ$ .

Taking the stars already selected according to their heliocentric distance, we now plot in Fig. 4 the observed proper motion in right ascension as a function of  $\tilde{\Lambda}_\odot$  (blue dots). We observe a modulation of the dispersion which is dominated by the correlation between the uncertainty and the distance. This is specially noticeable in the Strip sample (Fig. C.2), where the dispersion near the apocentres is significantly larger. Also, there are at least

<sup>5</sup> Downloaded from <http://faculty.virginia.edu/srm4n/Sgr/>

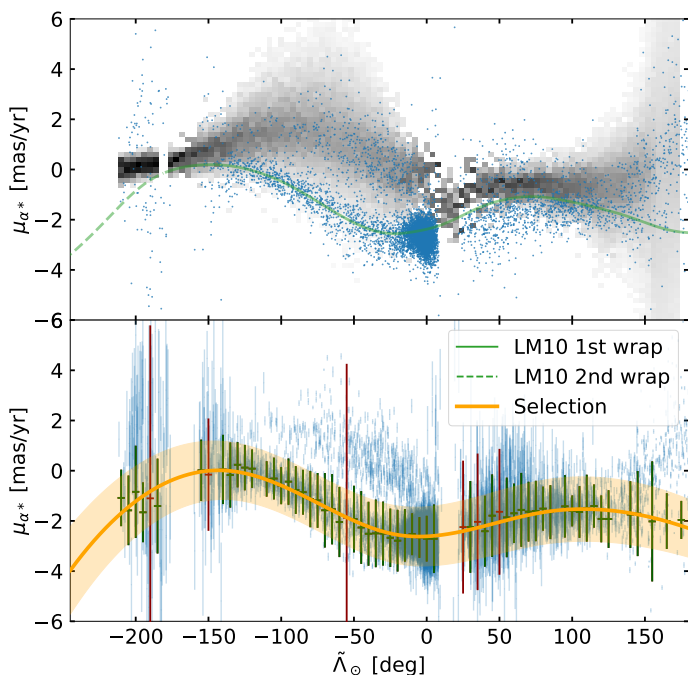


**Fig. 4.**  $\tilde{\Lambda}_{\odot}$  against proper motion in right ascension of the Sgr stream. Top: all stars selected by distance superimposed to the histogram obtained from the mock catalogue (see text). Bottom: result of the TGM (green and red error bars) and the area that we use to further filter out the contamination (orange). Here we also show, with green lines, the prediction of the LM10 model. The stars at the trailing apocentre have been moved to the left of the plot by subtracting  $-360^{\circ}$ .

two patterns clearly identifiable, specially at the beginning of the trailing and the leading arms.

To understand the effects of the contamination, we resort once more to the mock MW catalogue described in Sect. 3.3. For the mock sample, we use the orange area of the previous section to select by distance, then add the errors in proper motion provided with the mock catalogue and, finally, create the 2D histogram shown in the top panel of Fig. 4. As can be seen, it follows quite closely the trail of stars at higher  $\mu_{\alpha^*}$ . We note that these mock sources are all labelled as halo stars, except for the small range of  $\tilde{\Lambda}_{\odot}$  where the stream passes behind the Galactic Centre (GC), where it is dominated by thick disc stars with a small fraction of thin disc stars.

As for the distance, we run our TGM with the parameters listed in App.B and skip any bin that contains less than 5 stars since we have fewer left after the previous selection. The results are shown in the bottom panel of Fig. 4, where we can already see that the prediction of the LM10 model shown in the upper panel (green line) is similar to the trend we detect (see Sect 4.1 for a discussion on the residuals). Again, after selecting only the stars within the orange shaded area, we are left with 6 797 RR Lyrae (52 %) stars in the nGC3 sample. In the case of the Strip sample, we found that we cannot recover the same trend beyond  $\tilde{\Lambda}_{\odot} \geq 120^{\circ}$  due to the predominance of the contamination. We tried different parameter combinations without any success. Finally, to avoid leaving that region void, only beyond  $\tilde{\Lambda}_{\odot} = 120^{\circ}$  we select stars around the track of the LM10 model, choosing the ones with  $-3.5 \text{ mas yr}^{-1} \leq \mu_{\alpha^*} \leq -0.5 \text{ mas yr}^{-1}$  (orange box in Fig. C.2). This results in a list of 12 583 stars (16 %).

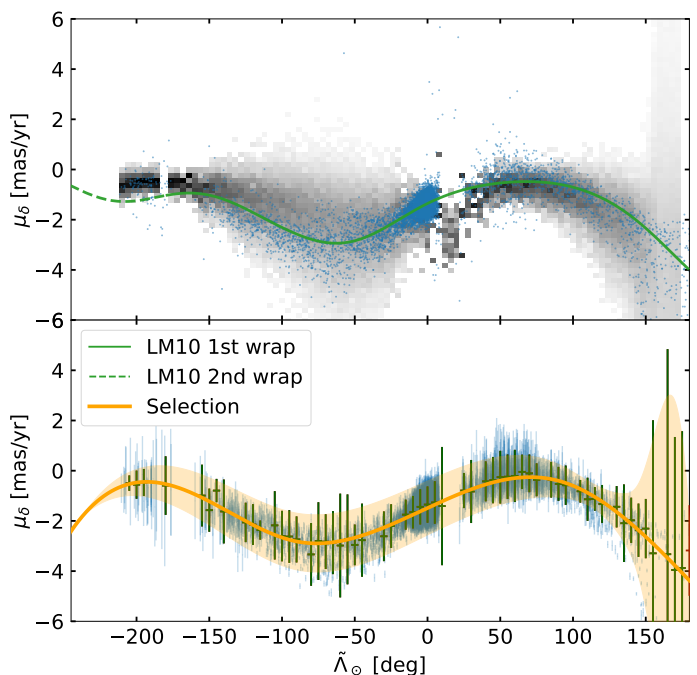


**Fig. 5.** Same as Fig. 4 but with proper motion in declination. Now we only show the stars selected by distance and  $\mu_{\alpha^*}$ .

### 3.5. Proper motion selection: Declination

We apply the TGM now to the proper motion in declination of the remaining stars with the same parameters as in Sect. 3.4 and basically recover a single component all along the stream, as can be seen in Fig. 5. We note that the halo stars from the mock catalogue present a proper motion that follows closely but not exactly that of the Sgr stream. This is likely due to the fact that  $\mu_{\delta}$  is roughly aligned with the motion perpendicular to the stream<sup>6</sup> and, since the dominant contribution in this direction is the Solar reflex, it is natural that the stream cannot be cleanly separated from the field. In this step, then, we have basically performed a 2-sigma clipping.

After applying these selections we obtain our final list of candidates with 6 608 stars for the nGC3 sample and 11 677 for the Strip. The two catalogues are available as one table at CDS, with a flag that describes whether the star was selected using one method, the other, or both.

## 4. Results

Now that we have assembled a reliable list of stars belonging to the Sgr stream, we proceed on to examine its main characteristics. In this section, in contrast with the previous, we focus on the Strip sample because, as we discuss below, the nGC3 presents a kinematical bias induced by the PCM method. The corresponding figures for the nGC3 sample can be found on Appendix D.

### 4.1. The missing dimensions: proper motions

First, we want to determine the proper motion of the Sagittarius stream and examine the two samples looking for the presence of any kinematic biases. We do so by comparing the trends in proper motion of our stars with those obtained by A20 and the

<sup>6</sup> The ICRS frame and the Sgr plane defined by Majewski et al. (2003) have similar poles.

predictions of LM10. In Fig. 6 (Fig. D.1) we present the proper motions in Galactic coordinates as a function of  $\tilde{\Lambda}_\odot$  for the Strip (nGC3) sample. The colours of the panels (a),  $\mu_l$ , and (b),  $\mu_b$ , as indicated by the colour bars, are the same as in Fig.3a of A20 to make comparisons easier. In panel (c), however, we show the total proper motion coloured by the distance derived for each RR Lyrae. In all three panels we have added the smooth median obtained from A20 (black) and the predictions of the LM10 model (green). We note that the farthest stars (blue points in panel c) roughly have the proper motion that the model predicts for the second wrap, confirming that we are indeed detecting the trailing tail's apocentre.

In panel (d) we plot the residuals between the median of A20 and the median of the Strip and nGC3 sample (computed in the same way), and the associated  $1\sigma$  intervals. This figure shows that even though the overall trends are similar, the discrepancy between A20 and the nGC3 sample exceeds  $3\sigma$  in the leading arm, becoming smaller as  $\tilde{\Lambda}_\odot$  increases. This is related to the lack of stars with small total proper motion in the nGC3 sample in that region. While this also seems to be the case for the Strip sample, here the discrepancy is within  $2\sigma$ . However, we note that the residuals start to grow again at  $\tilde{\Lambda}_\odot > 120^\circ$  in the Strip case, which is probably due to the degree of contamination being higher in this region due to our selection (see Sect. 3.4). In the trailing tail, the differences are within  $1\sigma$  until  $\tilde{\Lambda}_\odot \sim 125^\circ$ , at which point the A20 sample becomes heavily affected by the contamination of the disc. Remarkably enough, A20 has stars in the trailing apocentre, amid all the contamination, whose median  $\mu_{tot}$  is compatible with ours (orange shaded area), even though the only criteria used in their selection was based on proper motions. Overall, the differences are of the order of  $\sim 0.3 \text{ mas yr}^{-1}$  at most, and only with more accurate proper motions will we have the precision needed to assert whether there is a kinematic separation between the different populations within the stream.

We have also examined the residuals against LM10 (not shown here). For the case of the Strip sample, the agreement is within  $2\sigma$  in the range  $-150^\circ < \tilde{\Lambda}_\odot < 100^\circ$  only broken near the trailing apocentre, which is expected given the differences between the predicted distances and the observed ones (c.f. Fig. 3), and beyond  $L \geq 120^\circ$ , the region where we already know that the Strip selection is poor. In the case of the nGC3 sample, though, we observe a large discrepancy in proper motions at  $\tilde{\Lambda}_\odot \sim 40^\circ$  when compared to the model too. We also note significant residuals in the trailing arm, around  $\tilde{\Lambda}_\odot \sim 120^\circ$ . All together, we suspect that the use of the PCM method has introduced some bias. Indeed, when we apply nGC3 algorithm to the LM10 particles we observe a similar behaviour in the residuals, thus confirming that the nGC3 sample is kinematically biased. For this reason, we chose to study the mean properties of the stream with the Strip sample.

#### 4.2. Galactocentric distance

In Fig. 7, we show a decomposition of the Sgr stream into each of the available dimensions, with the first panel (a) containing the distribution of the candidate stars in the sky for reference. We begin by analysing the trend in Galactocentric distance with  $\tilde{\Lambda}_\odot$  by converting the heliocentric distances derived in Sect. 3.2 with the parameters of the Sun described in Sect. 3.1. We are interested in the distribution of the tidal debris across the Galaxy since it gives us a direct insight into the actual orbit of the progenitor (Binney & Tremaine 2008). Additionally, we also want to estimate the location of the apocentres and their angular separation, as this quantities are useful to characterise the stream and compare with independent determinations and models.

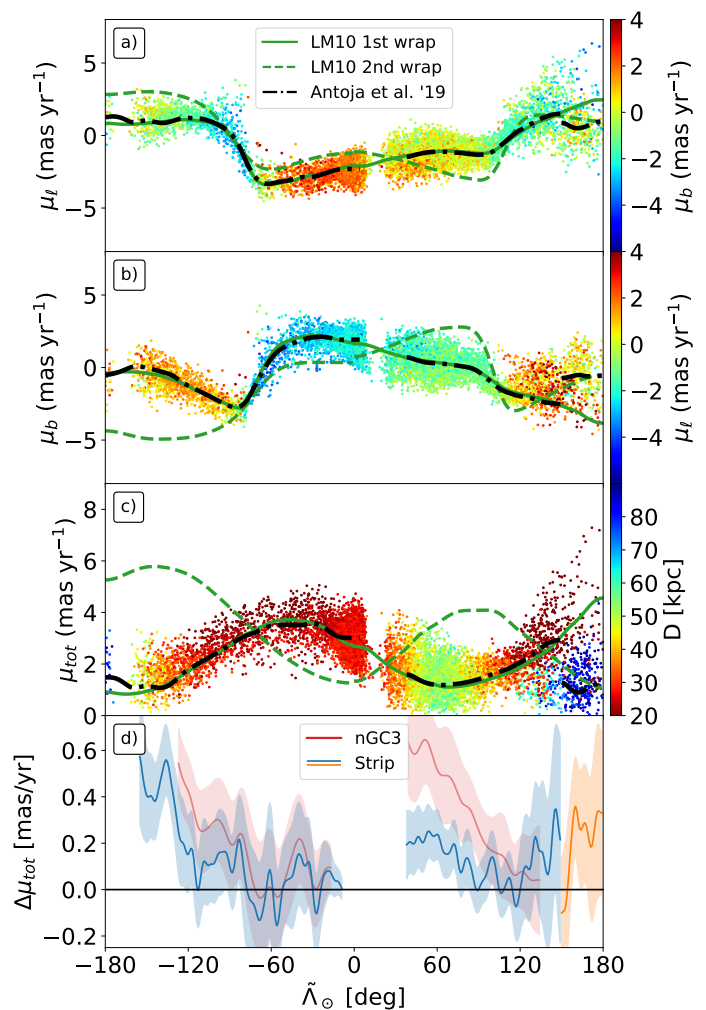


**Fig. 6.** Proper motion trends with  $\tilde{\Lambda}_\odot$  of the candidate RR Lyrae of the Sagittarius stream in the Strip sample. a) proper motion in Galactic longitude coloured by proper motion in Galactic latitude. b) same as above but swapping longitude by latitude. c) total proper motion coloured by distance. In all these panels we show the predictions from the LM10 model with solid (first wrap) and dashed (second wrap) green lines, as well as the smoothed median from A20 (dashed-dotted black line). Panel (d) contains the residuals between the smoothed median of the total proper motion for each of our final samples, nGC3 (red) and Strip (blue - first wrap, orange - second wrap), against A20.

as this quantities are useful to characterise the stream and compare with independent determinations and models.

We present in panel (b) of Fig.7 the Galactocentric distance distribution of the stars in the Strip sample as a function of  $\tilde{\Lambda}_\odot$ . In orange we show the smoothed median in bins of  $5^\circ$  and its associated  $1\sigma$  error. The green line corresponds to the prediction by LM10. We notice that the model does not follow our measurements, deferring more than  $3\sigma$  in most parts of the stream, including the centre of the dwarf. These discrepancies cannot be due to the metallicity zero-point assumed. We use Eq. 1 and 2 to convert the residuals in distance observed in the leading arm into differences in metallicity and we find that there should be a change of  $\sim 1$  dex in  $\sim 50^\circ$  to account for it. Obviously, this jump is much larger than the uncertainties in metallicity and would have been easily recognisable in Fig. 2. Moreover, the green and orange lines (model and data, respectively) cross at  $\tilde{\Lambda}_\odot \sim 30^\circ$  and again at  $\tilde{\Lambda}_\odot \sim 80^\circ$ , implying a change of sign in the residuals. This would require a shift as well in the sign of the offset ( $\Delta Z$

defined in Sect. 3.2) to explain it which, by construction, is not possible. Therefore it is safe to conclude that the deviations from the model are indeed physical. The same applies to the trailing arm, where the discrepancy in metallicity is too large to be artificial. On the other hand, the pattern we find is compatible with the determination made by Hernitschek et al. (2017) although, compared to their work, we do not use any modelling of the halo and, as a result, the trend that we recover is smoother.

We tried to calculate the apocentres using the recipe described in Belokurov et al. (2014) and used again in Hernitschek et al. (2017), which consists of describing the apocentres of the debris as a Gaussian profile. We find that fitting a Gaussian to the leading arm is not accurately reproducing our observations and the results are very dependent on the range of  $\tilde{\Lambda}_\odot$  used. Instead, we construct a cubic spline (orange line in 7.b) to smooth the median and obtain a curve that can be evaluated at any point. Then, we use it to search for the local maximum. Due to the underlying binning, we use half the bin-size in  $\tilde{\Lambda}_\odot$  as the uncertainty in the angular position. In distance, we use the error in the median shown as an orange shaded area in Fig. 7.b. The result of applying this strategy to the two samples is:

1. nGC3:
  - Trailing:  $\tilde{\Lambda}_\odot = -188^\circ \pm 2:5$  at  $D_{GC} = (93.22 \pm 2.39)$  kpc
  - Leading:  $\tilde{\Lambda}_\odot = 66^\circ \pm 2:5$  at  $D_{GC} = (47.34 \pm 0.58)$  kpc
2. Strip:
  - Trailing:  $\tilde{\Lambda}_\odot = -193^\circ \pm 2:5$  at  $D_{GC} = (92.48 \pm 1.45)$  kpc
  - Leading:  $\tilde{\Lambda}_\odot = 64^\circ \pm 2:5$  at  $D_{GC} = (47.73 \pm 0.48)$  kpc

with an angular distance between apocentres that implies a differential heliocentric orbital precession of  $\omega_\odot = 360^\circ + \tilde{\Lambda}_\odot^T - \tilde{\Lambda}_\odot^L = 103^\circ \pm 3:5$  (Strip).

The values we obtain for the nGC3 and Strip samples are compatible with one another, but we note that the angular positions in the trailing apocentre differ by one bin (i.e.,  $5^\circ$ ). Given that the nGC3 sample has few stars in that region, we expect the value inferred from the Strip to be more robust. We only show the statistical uncertainties but we stress again that a wrong metallicity zero-point would bias these estimates. Nevertheless, we expect the difference to be much smaller than 4% in distance (Sect. 3.2). On the other hand, the contribution of the uncertainty in the GC-Sun distance is negligible.

Our determination for the Strip, shown as vertical grey bands across the whole Fig. 7, has to be compared with the values derived by Belokurov et al. (2014):  $\tilde{\Lambda}_\odot = 71:3 \pm 3:5$  at  $D = (47.8 \pm 0.5)$  kpc for the leading arm and  $\tilde{\Lambda}_\odot = -189:5 \pm 1:0$  at  $D = (102.5 \pm 2.5)$  kpc for the trailing ( $\omega_\odot = 99:3 \pm 3:5$ ). We note that there is a  $\sim 3.5\sigma$  discrepancy at the far apocentre, which cannot be reconciled by tuning  $\Delta Z$  without creating tension in the near one. In contrast, the results of Hernitschek et al. (2017) using the RR Lyrae from PanSTARRS1 are closer to ours:  $\tilde{\Lambda}_\odot = 63:2 \pm 1:2$  at  $D = (47.8 \pm 0.5)$  kpc for the leading tail and  $\tilde{\Lambda}_\odot = -192:4 \pm 0:4$  at  $D = (98.95 \pm 1.4)$  kpc for the trailing ( $\omega_\odot = 104:4 \pm 1:3$ ). Nevertheless, the tension is still present. The major difference is that we have obtained our measurements in a model-independent way and using all the stars in our sample.

#### 4.3. A peek into the unknown: tangential velocities

Finally, with all 5 dimensions together (position, proper motion and distance) we can access an almost unexplored aspect of the stream: the tangential velocity. To do so, we make use of the *Python* package GALA (Price-Whelan 2017) which provides a tool to correct for the solar reflex given the position and velocity

of the Sun with respect to the GC. For that, we use the parameters described in Sect. 3. The resulting velocities for the Strip sample are shown in panels (c) and (d) of Fig. 7 for, respectively, the velocity along ( $v_{\tilde{\Lambda}_\odot}$ ) and across ( $v_{\tilde{B}_\odot}$ ) the stream. In contrast with the previous section, here we smooth the median values in bins of  $10^\circ$  in  $\tilde{\Lambda}_\odot$  with a Gaussian filter (similar to A20).

When looking at the velocity along the  $\tilde{\Lambda}_\odot$  axis (orange line in Fig. 7.c) we note the general agreement with the LM10 model (green line). In most of the regions both trends are compatible within  $3\sigma$  except for i) the dwarf itself, where we find that our results are  $\sim 20$  km s $^{-1}$  above the predictions and ii) beyond  $\tilde{\Lambda}_\odot > 80^\circ$ , where the differences exceed 70 km s $^{-1}$  at some points. While the later could be related with the contamination, said contamination would need to bias both the distance by more than 5 kpc and the proper motions by more than 0.3 mas yr $^{-1}$  to reconcile our observed  $v_{\tilde{\Lambda}_\odot}$  with the model. A more likely scenario is that the orbit of the progenitor in LM10 is not reproducing well the observations, which is consistent with our findings of Sect. 4.2 and with the fact that we observe a significantly different tangential velocity for the dwarf.

The velocity perpendicular to the orbital plane of Sgr is also interesting since it is where the effects of other satellites like the Magellanic Clouds are expected to be more noticeable. This is the case of the Orphan stream, where the misalignment between the velocities of the stars and its orbit have been related to the Large Magellanic Cloud (Erkal et al. 2019). In panel (d) we show the changes in  $v_{\tilde{B}_\odot}$  along the stream. We find no significant deviation from zero at the current level of precision but we notice the degeneracy with the velocities used to correct the solar reflex. Hayes et al. (2018) used a sample of Sgr stars to obtain an estimate of the Sun's velocity with respect to the galactic centre by fitting the observations to the model of LM10. Ideally, though, one would like to obtain a global fit that can quantify the deviations caused by the satellites at the same time that estimates the solar parameters. While our sample can indeed be used for that purpose, this analysis is out of the scope of the present work.

We can also obtain a measure of the total velocity projected in the sky of the Sgr dwarf that can be used to, for instance, initialise simulations from the present time. We do so by summing in quadrature both components of velocity for all stars within a cone of  $5^\circ$  around the centre of the Globular Cluster M54 (Bellazzini et al. 2008). Then, the median  $V_\perp$  and its uncertainty are:

1. nGC3:  $(274.18 \pm 0.02)$  km s $^{-1}$
2. Strip:  $(272.56 \pm 0.02)$  km s $^{-1}$

with the (small) difference between both samples being most likely caused by the larger fraction of contamination present in the Strip sample.

Our final output of this part is an interpolator for each component of the velocity for any  $\tilde{\Lambda}_\odot$  along the stream. Despite the large uncertainties in proper motions, we can still recover a trend that can be used to test future models of Sagittarius. In App. E we explain how to download them, along with the rest of interpolators used in this work: distance, proper motion, etc.

#### 4.4. Metallicity

Having a reliable sample of candidates, we can now check our initial assumption of a constant metallicity along the arms of Sgr (Sect. 3.2). In the fifth panel of Fig. 7 we show the metallicity distribution for the stars which have it measured. The error bars correspond to the median, with the associated error, in bins of  $30^\circ$  for both RRab (orange) and RRc (blue) type RR Lyrae. The first thing we note is that the median oscillates around the

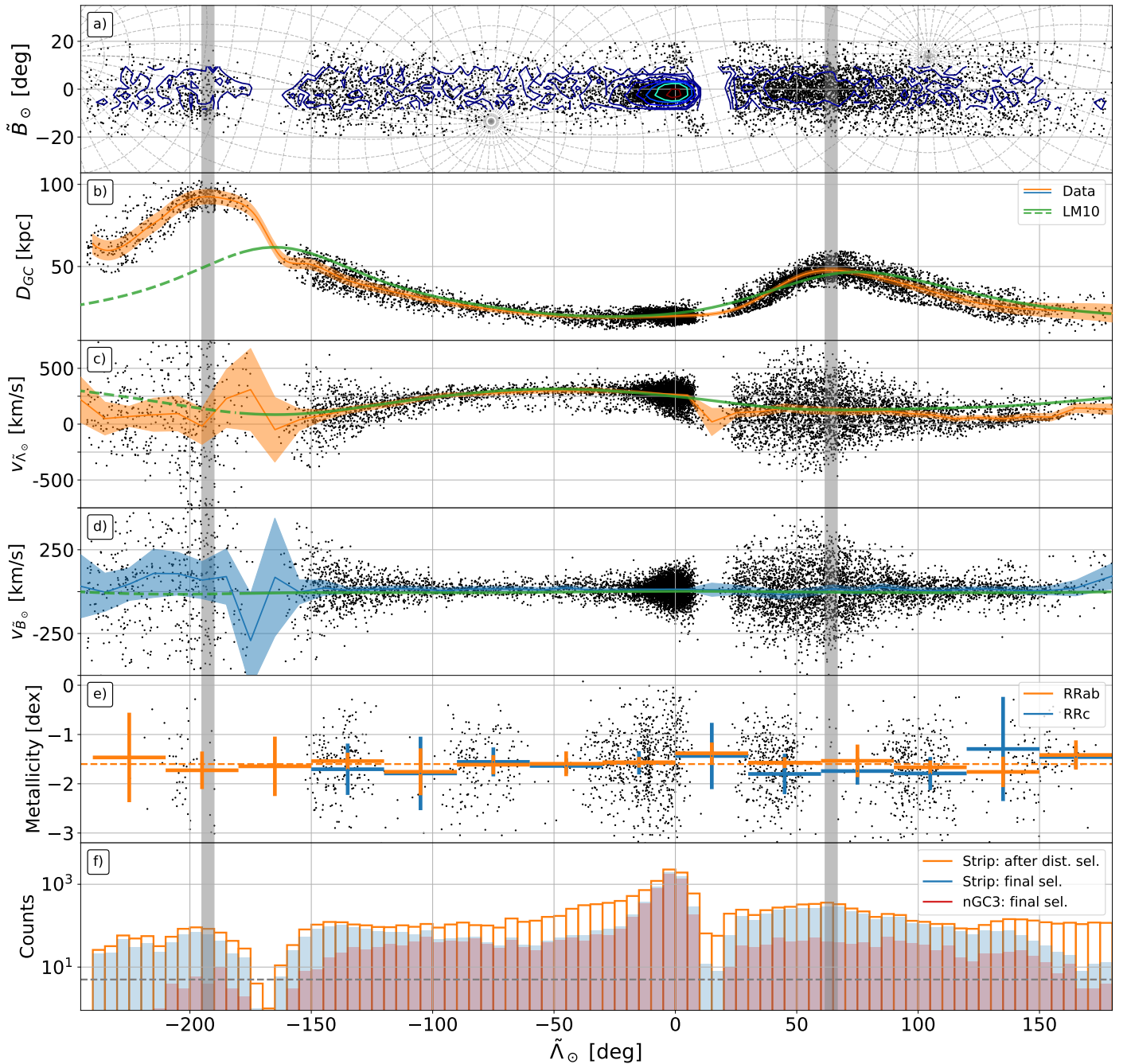


**Fig. 7.** Position, distance and velocities as a function of  $\tilde{\Lambda}_\odot$  of the Sgr stream (Strip sample). a) Sky distribution with overlaid count contours. The dashed lines represents a regular grid in the Galactic coordinate frame. b) Smoothed median (orange line) and associated uncertainty (orange area) of the Galactocentric distance for the data (black dots) and LM10 (green line). c-d) Same as (b) but for the velocity in the  $\tilde{\Lambda}_\odot$  (orange) and  $\tilde{B}_\odot$  (blue) directions after correcting for the solar reflex. e) Median metallicity of the RR Lyrae types AB (orange) and C (blue). f) Histograms of  $\tilde{\Lambda}_\odot$  for the Strip sample – but only after selecting by distance – (orange), for the final Strip sample (blue) and for the nGC3 sample (red). The dashed black line represents the threshold below which we do not compute the median used in the other panels. We also show as two vertical grey stripes the positions of the apocentres (see text).

dashed line that represents the mean value calculated previously in Sect. 3.2 with all stars in the range of distance between 20 kpc and 50 kpc:  $-1.6$  dex.

Already with this we can clearly see that there is no appreciable gradient. Nevertheless, we measure it by fitting a line to all RRab stars in the leading ( $\tilde{\Lambda}_\odot > 0^\circ$ ) and the trailing ( $\tilde{\Lambda}_\odot < 0^\circ$ ) arms. By doing so we obtain a slope of, respectively,  $(-1.8 \pm 0.5) \times 10^{-3}$  dex  $\text{deg}^{-1}$  and  $(0.3 \pm 0.4) \times 10^{-3}$  dex  $\text{deg}^{-1}$ . In the case of the nGC3 sample, the result is  $(-2.3 \pm 0.7) \times 10^{-3}$  dex  $\text{deg}^{-1}$  in the leading arm and

$(1.2 \pm 0.6) \times 10^{-3}$  dex  $\text{deg}^{-1}$  in the trailing. While this could be easily disregarded as unimportant, we note that the current estimates of the metallicity gradient in the tails of Sgr are of the order of  $10^{-3}$  dex  $\text{deg}^{-1}$  (Hayes et al. 2019). Nevertheless, considering the inhomogeneous coverage of the sky of the subsample of stars with metallicity and the possible contribution from the contamination, it is hard to trust the variations that we measure. In the worst case scenario, this would cause a difference at the trailing apocentre of  $\sim 0.2$  dex, of the order of the precision achievable with photometric metallicities. In turn, such differ-

**Table 2.** Metallicity statistics of the nGC3 (Strip) final sample. We show for each type of RR Lyrae (first column): the number of sources classified as such with reported metallicity (second column), their mean metallicity as given in the *Gaia* archive (third column) and the associated standard deviation (fourth column).

Type	N	$\langle[\text{Fe}/\text{H}]\rangle$ [dex]	$\sigma_{[\text{Fe}/\text{H}]}$ [dex]
RRab	997 (1 876)	-1.60 (-1.62)	0.63 (0.62)
RRc	89 (149)	-1.62 (-1.65)	0.45 (0.46)
RRd	1 (2)	-1.11 (-1.10)	- (0.02)

ence would imply that our measurement of the distance obtained in the previous section could be short by  $\sim 3\%$ , i.e. that the trailing apocentre could be in fact at a distance of  $\sim 96$  kpc instead of  $\sim 93$  kpc. While this effect would bring our estimate closer to the values in the literature<sup>7</sup>, it is still within its  $2\sigma$  confidence interval. In summary, we can say that, effectively, there is no measurable metallicity gradient at the current level of precision offered by the photometric metallicities.

Finally, we show the mean values of metallicity for each type of RR Lyrae star in Table 2 from which we can conclude that the metallicity of this sample is  $-1.61 \pm 0.01$  dex.

#### 4.5. Completeness assessment

Here, we inspect the distribution of the counts along the stream and the overlap between the different samples. The bottom panel of Fig. 7 shows the number of stars of the final Strip sample (blue bars) in  $5^\circ$  bins, compared to the counts after the selection based on distance of Sect. 3.3 (orange step). Here, the dashed black line represents the imposed limit of 5 stars below which we do not compute the median used in panels (b), (c) and (d).

As expected, a significant fraction of the stars fall inside the dwarf itself: 4 730 (40%) in the region  $\tilde{\Lambda}_\odot \in [-10^\circ, 10^\circ]$ . The rest are spread rather uniformly except for the two parts where the stream crosses behind the MW disc, easily identifiable by a sudden drop in the counts. We do observe a larger amount of stars in the leading arm compared to the symmetric  $\tilde{\Lambda}_\odot$  in the trailing, which is to be expected near apocentre where the stars in the stream slow down. Nevertheless, as explained in Sect. 3.4, the increase of the proper motion uncertainties near apocentre prevents us from effectively reducing the contamination there. That is why the orange (Strip sample after selecting only based on distance) and blue (final Strip sample) histograms are so close to each other in that region.

We also include the counts of the final nGC3 sample as red bars. In this case, the two distributions are similar for  $\tilde{\Lambda}_\odot < 0^\circ$  but more different for the leading arm. The cross-match between both final samples tells us that all stars in the nGC3 sample, except for 44 stars, are in the Strip sample. Thus, the missing stars in the leading tail are those that cause the difference in total proper motion seen in Fig. 6. Comparing both samples, we note that Cseresnjes (2001) estimated the total amount of RRab stars to be  $\sim 8 400$ . This value is right between the number of stars in the nGC3 and Strip sample, reinforcing the idea that the former is pure but incomplete and the later complete but contaminated.

We have also cross-matched our two samples to that of A20. The first thing that is important to mention is that A20 contains only 3 476 RR Lyrae of the 182 495 in the list presented in Sect. 2. Compared to our two samples, A20 contains 3 233

<sup>7</sup> If we consider the gradient in both tails, then the estimate of the distance at the leading apocentre grows to  $\sim 48.5$  kpc, departing from the values estimated by previous authors.

of the 11 677 in the Strip and 2 712 stars of the 6 608 in the nGC3 sample. If we restrict ourselves to the region where the contamination is lower ( $-120^\circ < \tilde{\Lambda}_\odot < 150^\circ$ ) then we get that, out of the 3 145 RR Lyrae in A20, 3 033 are among the 10 431 of the Strip sample. For the nGC3 sample, we obtain a cross-match of 2 661 out of 6 386 stars. This means that the recovery fraction of our two catalogues is around 95% for the Strip and around 80% for the nGC3. Since we obtained these estimates from low-contamination regions, we expect them to be similar to the true completeness but we stress that this percentages apply only to the true members among all the candidates (as if there was no contamination). In any case, the RR Lyrae in A20 that are *not* in any of our two samples can mostly be found in the dwarf, the tip of the tails (where we know that the contamination in A20 is higher) and, most interestingly, the leading apocentre. Investigating further the differences among the samples, though, requires a fine characterisation of the different selection functions and we leave it for a future study. On the other hand, the recovery fraction for the RR Lyrae in A20 is roughly between 30% and 40% (we cannot extrapolate this estimates of completeness to stars with other colours and magnitudes). Engrossing the list of A20, though, would require a good treatment of the contamination and probably the introduction of a model for the halo and thin/thick disc.

#### 4.6. Velocity dispersion

As mentioned in Gibbons et al. (2014), the stars that escape through the Lagrange points do so with a dispersion in velocity inherited from the dispersion that the stars had at the outskirts of the dwarf, the later being proportional to the total mass of the infalling satellite. Additionally, the stream can get kinematically heated by the continuous interaction with dark matter sub-halos (Johnston et al. 2002). Therefore, learning about the velocity dispersion of the stream allows us to obtain a tighter constrain on the dynamical mass of the progenitor and, potentially, a test for dark matter models.

In Fig. 8 we show the velocity dispersion profile of  $v_{\tilde{B}_\odot}$  for both the Strip sample (orange) and the nGC3 (red). We also include the profile of the LM10 model in green (solid line). We have been able to reproduce both curves easily with the LM10 particles by randomly assigning the uncertainties of the observed stars (dashed) and subsequently applying the nGC3 PCM method (dashed-dotted). The remaining differences between the observed profiles and the ones predicted by the model are mostly due to the fact that we did not apply the whole methodology described in Sect. 3.3 to 3.5. If we wanted to obtain an estimate of the deviations caused by possible sub-halos, it would be necessary to build the selection function of our two sample and model accurately the observational errors.

#### 4.7. The Bifurcation

The bifurcation of the Sgr stream was observed for the first time by Belokurov et al. (2006) in the leading tail, and later detected in the trailing arm by Koposov et al. (2012) and Navarrete et al. (2017). This feature can be clearly seen with the M giants and shows the stream splitting into two branches creating a bi-modal distribution of  $\tilde{B}_\odot$  in some portions of the tails. Although some models have been proposed to explain this feature with only one progenitor, e.g. Peñarrubia et al. (2010) (but see Peñarrubia et al. 2011), there is no consensus on its cause. Thus, it is important to

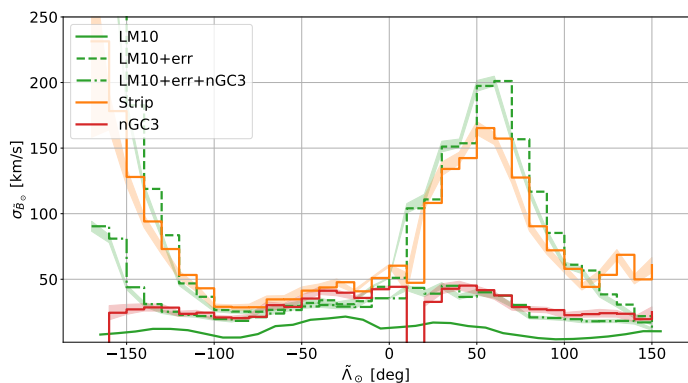


**Fig. 8.** Velocity dispersion as a function of  $\tilde{\Lambda}_\odot$  across the stream. The orange (red) steps correspond to the velocity dispersion observed in the final Strip (nGC3) sample. The green lines are the LM10 model: the solid is for the model particles, the dashed for the model after introducing the observed errors in proper motion and the dashed-dotted, the same but after applying the nGC3 method (see text).

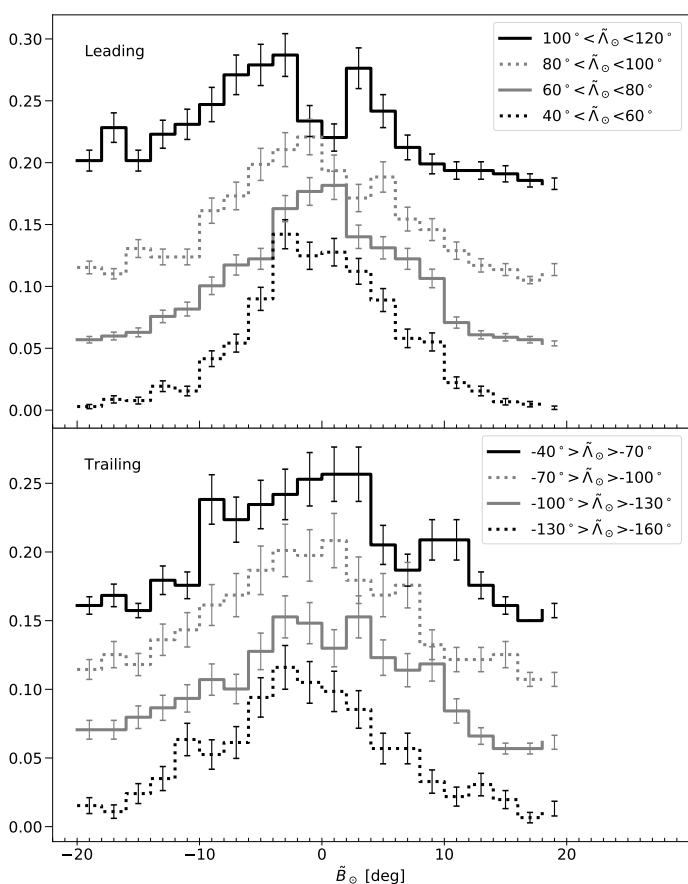


**Fig. 9.** Normalised histogram of  $\tilde{B}_\odot$  for different bins of  $\tilde{\Lambda}_\odot$  for the Strip final sample. Top: bins in the leading arm. Bottom: bins in the trailing arm. We have added an arbitrary offset in the y-axis to each curve for visualisation purposes.

provide additional observational evidence with different tracers to constrain the range of possibilities.

Figure 9 shows the histogram of  $\tilde{B}_\odot$  of the final Strip sample for different bins in  $\tilde{\Lambda}_\odot$  within the range  $-160^\circ < \tilde{\Lambda}_\odot < 120^\circ$ . In some portions of the leading arm (top panel) a bi-modal distribution is evident. The strongest signal is in the range  $100^\circ < \tilde{\Lambda}_\odot < 120^\circ$ , where the two highest peaks are separated by  $\sim 6^\circ$ . We note the agreement between our findings and those

in Belokurov et al. (2006), where they report the beginning of the bifurcation at  $\tilde{\Lambda}_\odot \sim 80^\circ$  and the separation between the two branches growing from  $\sim 7^\circ$  to  $\sim 10^\circ$  at  $\tilde{\Lambda}_\odot \sim 120^\circ$ . The bifurcation is also evident in the nGC3 sample (see Fig. D.2). In the trailing arm there is no bifurcation appreciable. We have increased the bin width to compensate for the lower number of counts, but still we cannot see a significant signal (bottom panel of Fig. 9).

To investigate the possible differences between the two branches observed in the leading arm, we compute the weighted means for the distance and proper motions in four bins of  $\tilde{\Lambda}_\odot$ :  $90^\circ$  to  $100^\circ$ ,  $100^\circ$  to  $110^\circ$ ,  $110^\circ$  to  $120^\circ$  and, finally,  $120^\circ$  to  $130^\circ$ . The weight assigned to each star represents the probability of belonging to one branch or the other based on their  $\tilde{B}_\odot$ . To obtain these two probability distribution functions, first we create a kernel of  $\tilde{B}_\odot$  to have a continuous representation of the histogram. Then, we locate the only two local maxima that the kernel has and associate each one with either branch A (negative  $\tilde{B}_\odot$ ) or branch B (positive  $\tilde{B}_\odot$ ). After that, we restrict ourselves to  $\pm 1.5^\circ$  of one of the peaks, i.e. we only use the values of the kernel near the local maxima, and fit a parabola with which we can obtain a probability at every  $\tilde{B}_\odot$  (obviously, wherever the parabola returns a negative probability we instead use zero). Finally, we repeat for the other peak to obtain the second probability distribution. Figure 10 shows, in panels (a) to (d), the original histogram of  $\tilde{B}_\odot$  at each bin in  $\tilde{\Lambda}_\odot$  (black line) along with the resulting weighted histograms for branches A (blue) and B (orange). Panels (e) to (g) contain the corresponding weighted averages and their  $1\sigma$  uncertainties in heliocentric distance, proper motion in right ascension and proper motion in declination, respectively. To compute the uncertainty in this estimate, i.e. standard error of the weighted mean (SEM), we have used the formalism of Cochran (1977)<sup>8</sup>. In order to cancel the gradients observed in the previous sections, we subtract the median value obtained from the stars within the bin.

The result is that the differences that we measure between the two sides of the bifurcation are always smaller than  $2\sigma$ . Nevertheless, we note that the orange line in panel (e) is always below the blue one. This can be due to many factors like projection effects, caused by the stream being an actual 3D structure, or contamination, since the faint branch (B) is more susceptible than the bright branch (A), or simply because one branch is actually more extinguished than the other, which could be not well reproduced with the extinction map that we use. As an example, supposing that the later is true, we would only need to add  $< 0.1$  mag of extinction to the mean distance of branch A to bring the blue line in panel (e) down to the orange line.

In contrast with the recent study of Yang et al. (2019), where they report differences in velocity and metallicity for Blue Horizontal Branch stars in the bifurcation, we conclude that there is no significant separation in either kinematics or distance between the two branches of the leading tail. And if there were, these should be of the order of  $< 1.5$  kpc and  $< 0.2$   $\text{mas}^{-1}$ . We have also looked at the metallicity and find no significant difference but, due to the small number of stars available and the measurement errors, we cannot give any meaningful upper limit. Finally, the fact that we do not observe the bifurcation in the trailing tail could be related either to our selection function or simply to a lack of stars.

<sup>8</sup>  $(SEM_w)^2 = \frac{n}{(n-1)\sum \omega_i} [\sum (\omega_i x_i - \bar{\omega} \bar{x}_w)^2 - 2\bar{x}_w \sum (\omega_i - \bar{\omega})(\omega_i x_i - \bar{\omega} \bar{x}_w) + \bar{x}_w^2 \sum (\omega_i - \bar{\omega})^2]$

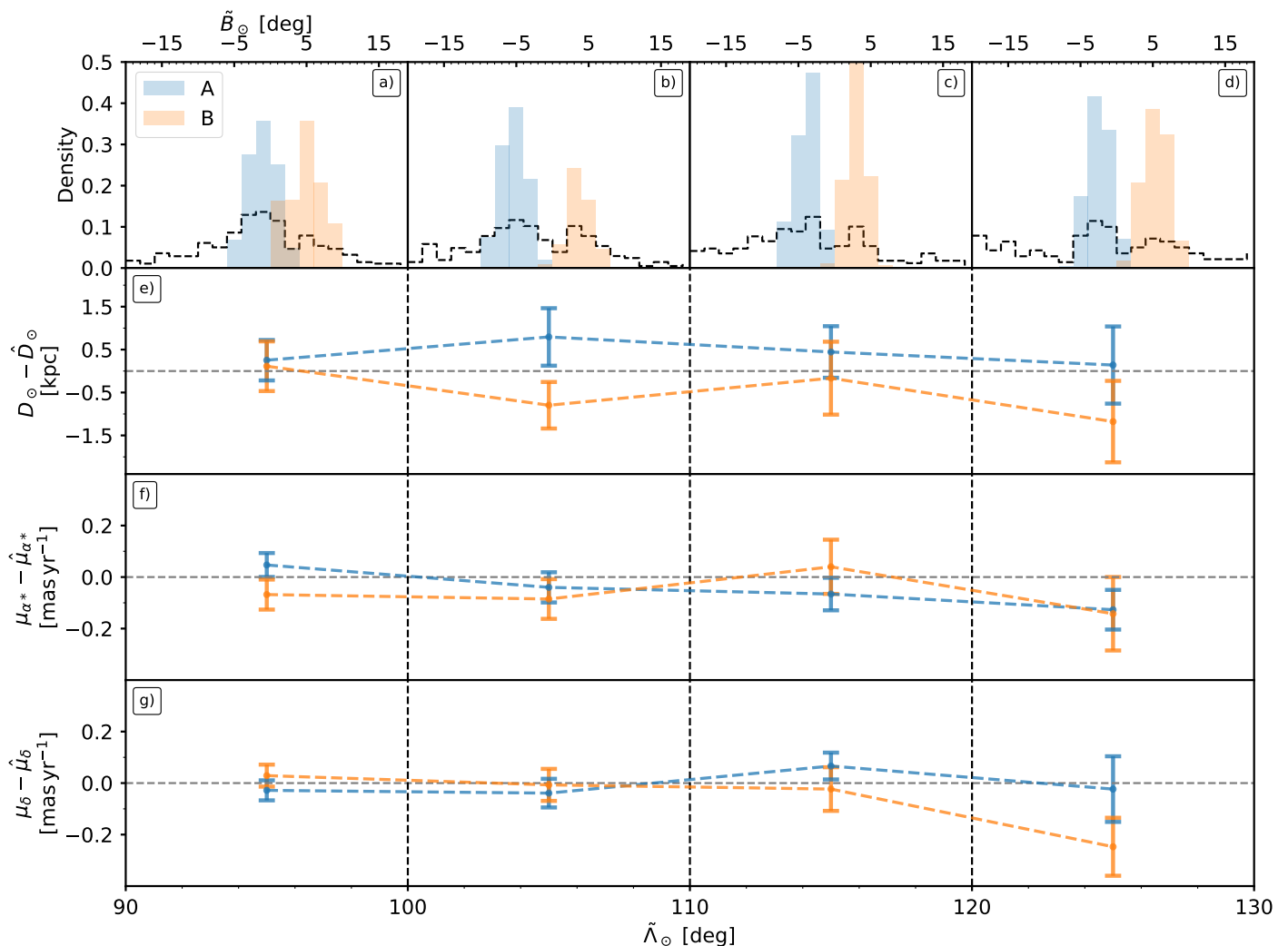


**Fig. 10.** Comparison between the bright (A, blue) and faint (B, orange) branches of the bifurcation at different  $\tilde{\Lambda}_0 > 90^\circ$  (Strip sample). On the top panels (a) to (d), we show the histogram of  $\tilde{B}_0$  (black line) corresponding to the stars that fall in the range of  $\tilde{\Lambda}_0$ , from left to right,  $[90^\circ\text{-}100^\circ, 100^\circ\text{-}110^\circ, 110^\circ\text{-}120^\circ, 120^\circ\text{-}130^\circ]$ . We also show the weighted histograms for each branch, that illustrate which are the stars that contribute to compute the means plotted in the panels below. In panel (e) we plot the weighted mean heliocentric distance, after subtracting the median distance, and the associated error. Panels (f) and (g) contain the weighted mean and its error for, respectively, the proper motion in right ascension and in declination. Here we also subtract the median value of the bin to cancel the overall gradients.

## 5. Conclusions

*Gaia* has revolutionised the field of Galactic astronomy. With only 22 months of data, the scientific community has already been able to make numerous and quite significant discoveries. Nonetheless, DR2 can produce amazing results even when dealing with things that we supposedly had a good handle on. The Sgr stream is a good example of that and in this work, as well as in A20, we wanted to demonstrate how its discovery would have been like in the *Gaia* era.

We have produced two catalogues of probable RR Lyrae members of the Sgr dwarf and stream, starting with the most basic assumptions and squeezing the *Gaia* outputs to carefully prune the list of candidates step by step. The two catalogues are produced by running this trimming process twice, each time from a different starting point. In the first case, we look for stars that are rotating coherently in a plane through the Galactic Centre and end-up with the nGC3 sample: a higher-purity, but lower-completeness ( $\approx 80\%$ ) sample. By demanding that the stars and their velocities do not deviate significantly from the mean orbital plane, we are able to discard efficiently most of the contamina-

tion at the cost of introducing kinematical biases. The second time, we select all stars in the sky that are within  $\pm 20^\circ$  from the stream's known mid-plane. In doing so, we obtain the Strip sample: a higher-completeness ( $\approx 95\%$ ), but lower-purity sample. In this case, we rely on our data-driven selection schema based on distances and proper motions to drop most of the contamination. We have composed a list of 11 721 stars belonging to either the Strip (11 677 stars) or the nGC3 (6 608 stars) sample, publicly available.

The main output of this work is the largest sample of RR Lyrae in the Sgr stream to date with both proper motions and distances together. This allows us to study, for the first time, the tangential velocities along the whole stream and provide a reference to compare against. Our results confirm the findings by A20 regarding the proper motion track along the stream. We observe effectively the same trends in proper motion, with differences of less than 0.3 mas/yr in most parts of the stream. The exception are only those regions where either our sample or that of A20 are known to be contaminated. Also, we note that 93% of the RR Lyrae contained in A20 are inside our final sample confirming that both are detecting the same structure. It will be interesting

to compare our work with that of Ibata et al. (private communication) in which, as we recently found out, they also provide a list of RR Lyrae obtained with *STREAMFINDER* (Malhan & Ibata 2018). In doing so, we can produce an independent estimate of the completeness as well as quantify the possible biases.

We compare the evolution of the different observables with  $\tilde{\Lambda}_{\odot}$  against LM10, the reference model for most studies of Sgr. The residuals in proper motion are within the uncertainties, apart from the known issues discussed in Sect. 4. That is, that the Strip's mean  $\mu_{\alpha^*}$  is not reliable beyond  $\tilde{\Lambda}_{\odot} > 120^{\circ}$  and that the nGC3 sample is biased. When comparing the heliocentric distances, we find that the discrepancies are very much significant and not attributable to a gradient in metallicity or a wrong calibration. Instead, we confirm the results of previous works (e.g., Belokurov et al. 2014; Hernitschek et al. 2017) which already pointed out that the apocentres in LM10 are off in both  $\tilde{\Lambda}_{\odot}$  and distance. More recent models, like the one by Fardal et al. (2019), are able to reproduce this but it is yet to be tested how well do their proper motions perform in the light of the new observational constraints that we are providing. We have also determined new apocentres based on the maximum Galactocentric distance of the tidal debris:  $\tilde{\Lambda}_{\odot} = -193^{\circ} \pm 2.5^{\circ}$  at  $D_{GC} = (92.48 \pm 1.45)$  kpc for the trailing tail and  $\tilde{\Lambda}_{\odot} = 64^{\circ} \pm 2.5^{\circ}$  at  $D_{GC} = (47.73 \pm 0.48)$  kpc for the leading. Our values are in some tension with those determined by Hernitschek et al. (2017) which cannot be explained by a wrong metallicity zero-point, and are most likely related to the fact that we used a completely empirical method to estimated said apocentres.

With the Strip sample, we have been able to test the tangential velocities predicted by LM10. We find that the predictions agree within uncertainties in the trailing arm but fail to reproduce our observations at the location of the dwarf and at the leading arm. Moreover, we provide a measurement of the total velocity projected in the sky for the progenitor,  $V_{\perp} = (274.18 \pm 0.02)$  km s<sup>-1</sup>. Despite the complexity of our selection process, we can add that the velocity dispersion profiles of the model are also compatible with our observations.

Regarding the metallicity, we do not observe any meaningful gradient with  $\tilde{\Lambda}_{\odot}$  at the current level of precision and the mean value we recover is -1.6 dex in the ZW84 scale. This contrasts with other studies where they detect differences for most populations. In particular Yang et al. (2019) has reported a significant difference between the leading and the trailing arm for the Blue Horizontal Branch stars. Even though we use photometric metallicities instead of spectroscopic, the former having larger uncertainties, the hypothetical gradient has to be, in absolute value, of the order of  $10^{-3}$  dex deg<sup>-1</sup> at most. Such small gradients would cause differences along the stream no larger than  $\sim 0.2$  dex, which is similar to the typical precision for the photometric metallicities. We notice, though, that the gradients that we have measured, compatible with the values obtained by Hayes et al. (2019), would imply that the trailing arm is on average slightly more metal rich than the leading arm, in agreement with previous works (e.g., Yang et al. 2019).

The nGC3 sample is a great starting point for a spectroscopic follow-up. Taking advantage of its high purity, the risk of measuring abundances and radial velocities for an off-stream star is minimised. The resulting catalogue would be the most extensive 6D+abundance sample of Sgr RR Lyrae, providing a deeper look into the metallicity of the stream and probing the full phase-space information for a single tracer.

We have also searched for the bifurcation in our data and we indeed observe it in both samples. We see a clear signal in the leading arm, where it was originally discovered. We observe no

significant separation in velocity, distance or metallicity between the bright and faint branches. Also, we do not detect the bifurcation on the trailing arm where it was found by Koposov et al. (2012), perhaps due to the low number of stars we have in that region or because of the filters in distance and proper motion used to select the members. It will be interesting to obtain follow-up spectroscopic observations of the stars at each branch and study whether there is or not a separation in line of sight velocities as well.

Finally, we provide empiric trends (smoothed medians) in distance, proper motion and tangential velocities of our final Strip sample (see Sect. E), along with the respective uncertainties. We also give these trends as interpolators that can be evaluated at any  $\tilde{\Lambda}_{\odot}$  which can be very helpful in the modelling of the stream.

*Acknowledgements.* We thank J.M. Carrasco and Bertrand Lemasle for the useful comments and discussions, as well as the whole *Gaia* team at Barcelona and Groningen. This work has made use of data from the European Space Agency (ESA) mission *Gaia* (<https://www.cosmos.esa.int/gaia>), processed by the *Gaia* Data Processing and Analysis Consortium (DPAC, <https://www.cosmos.esa.int/web/gaia/dpac/consortium>). Funding for the DPAC has been provided by national institutions, in particular the institutions participating in the *Gaia* Multilateral Agreement. This project has received funding from the University of Barcelona's official doctoral program for the development of a R+D+i project under the APIF grant and from the European Union's Horizon 2020 research and innovation programme under the Marie Skłodowska-Curie grant agreement No. 745617. This work was supported by the MINECO (Spanish Ministry of Economy) through grants ESP2016-80079-C2-1-R (MINECO/FEDER, UE) and ESP2014-55996-C2-1-R (MINECO/FEDER, UE) and MDM-2014-0369 of ICCUB (Unidad de Excelencia 'María de Maeztu'). This project has received support from the DGAPA/UNAM PAPIIT program grant IG100319. The work reported on in this publication has been fully or partially supported by COST Action CA18104: MW-Gaia. CM acknowledges support from the ICC University of Barcelona visiting academic grants and thanks the *Gaia* UB team for hosting her during part of this research. CM also thanks PDU en Ciencias Físicas at CURE (Rocha), for their hospitality.

## References

- Abedi, H., Mateu, C., Aguilar, L. A., Figueras, F., & Romero-Gómez, M. 2014, *MNRAS*, 442, 3627
- Antoja, T., Ramos, P., Mateu, C., et al. 2020, arXiv e-prints, arXiv:2001.10012
- Bellazzini, M., Ibata, R. A., Chapman, S. C., et al. 2008, *AJ*, 136, 1147
- Belokurov, V., Koposov, S. E., Evans, N. W., et al. 2014, *MNRAS*, 437, 116
- Belokurov, V., Zucker, D. B., Evans, N. W., et al. 2006, *ApJ*, 647, L111
- Binney, J. & Tremaine, S. 2008, *Galactic Dynamics: Second Edition*
- Camarrillo, T., Mathur, V., Mitchell, T., & Ratna, B. 2018, *PASP*, 130, 024101
- Cardelli, J. A., Clayton, G. C., & Mathis, J. S. 1989, *ApJ*, 345, 245
- Catelan, M. & Smith, H. A. 2015, *Pulsating Stars*
- Chambers, K. C., Magnier, E. A., Metcalfe, N., et al. 2016, arXiv e-prints, arXiv:1612.05560
- Clementini, G., Ripepi, V., Molinaro, R., et al. 2019, *A&A*, 622, A60
- Cochran, W. G. 1977, *Sampling Techniques*, 3rd Edition. (John Wiley)
- Cseresnjes, P. 2001, *A&A*, 375, 909
- de Boer, T. J. L., Belokurov, V., & Koposov, S. 2015, *MNRAS*, 451, 3489
- Deg, N. & Widrow, L. 2013, *MNRAS*, 428, 912
- Di Fabrizio, L., Clementini, G., Maio, M., et al. 2005, *A&A*, 430, 603
- Duffau, S., Zinn, R., Vivas, A. K., et al. 2006, *ApJ*, 636, L97
- Erkal, D., Belokurov, V., Laporte, C. F. P., et al. 2019, *MNRAS*, 487, 2685
- Eyer, L., Mowlavi, N., Evans, D. W., et al. 2017, ArXiv e-prints [arXiv:1702.03295]
- Fardal, M. A., van der Marel, R. P., Law, D. R., et al. 2019, *MNRAS*, 483, 4724
- Gaia* Collaboration, Brown, A. G. A., Vallenari, A., et al. 2018, *A&A*, 616, A1
- Gaia* Collaboration, Prusti, T., de Bruijne, J. H. J., et al. 2016, *A&A*, 595, A1
- Gibbons, S. L. J., Belokurov, V., Erkal, D., & Evans, N. W. 2016, *MNRAS*, 458, L64
- Gibbons, S. L. J., Belokurov, V., & Evans, N. W. 2014, *MNRAS*, 445, 3788
- Gratton, R. G., Bragaglia, A., Clementini, G., et al. 2004, *A&A*, 421, 937
- Grillmair, C. J. & Carlin, J. L. 2016, in *Astrophysics and Space Science Library*, Vol. 420, Tidal Streams in the Local Group and Beyond, ed. H. J. Newberg & J. L. Carlin, 87
- Harris, W. E. 1996, *AJ*, 112, 1487
- Hayes, C. R., Law, D. R., & Majewski, S. R. 2018, *ApJ*, 867, L20

- Hayes, C. R., Majewski, S. R., Hasselquist, S., et al. 2019, arXiv e-prints, arXiv:1912.06707
- Hernitschek, N., Sesar, B., Rix, H.-W., et al. 2017, *ApJ*, 850, 96
- Holl, B., Audard, M., Nienartowicz, K., et al. 2018, *A&A*, 618, A30
- Ibata, R. A., Gilmore, G., & Irwin, M. J. 1994, *Nature*, 370, 194
- Ibata, R. A., Malhan, K., & Martin, N. F. 2019, *ApJ*, 872, 152
- Johnston, K. V., Hernquist, L., & Bolte, M. 1996, *ApJ*, 465, 278
- Johnston, K. V., Spergel, D. N., & Haydn, C. 2002, *ApJ*, 570, 656
- Jurcsik, J. & Kovacs, G. 1996, *A&A*, 312, 111
- Jurić, M., Ivezić, Ž., Brooks, A., et al. 2008, *ApJ*, 673, 864
- Koleva, M., Prugniel, P., De Rijcke, S., & Zeilinger, W. W. 2011, *MNRAS*, 417, 1643
- Koposov, S. E., Belokurov, V., Evans, N. W., et al. 2012, *ApJ*, 750, 80
- Koposov, S. E., Belokurov, V., Li, T. S., et al. 2019, *MNRAS*, 485, 4726
- Law, D. R. & Majewski, S. R. 2010, *ApJ*, 714, 229
- Li, J., FELLOW, L., Liu, C., et al. 2019, *ApJ*, 874, 138
- Liu, C., Deng, L.-C., Carlin, J. L., et al. 2014, *ApJ*, 790, 110
- Majewski, S. R., Skrutskie, M. F., Weinberg, M. D., & Ostheimer, J. C. 2003, *ApJ*, 599, 1082
- Malhan, K. & Ibata, R. A. 2018, *MNRAS*, 477, 4063
- Martínez-Delgado, D., Gómez-Flechoso, M. Á., Aparicio, A., & Carrera, R. 2004, *ApJ*, 601, 242
- Mateo, M., Mirabal, N., Udalski, A., et al. 1996, *ApJ*, 458, L13
- Mateu, C., Bruzual, G., Aguilar, L., et al. 2011, *MNRAS*, 415, 214
- Mateu, C., Cooper, A. P., Font, A. S., et al. 2017, *MNRAS*, 469, 721
- Mateu, C., Read, J. I., & Kawata, D. 2018, *MNRAS*, 474, 4112
- Mateu, C. & Vivas, A. K. 2018, *MNRAS*, 479, 211
- Mateu, C., Vivas, A. K., Downes, J. J., et al. 2012, *MNRAS*, 427, 3374
- Muraveva, T., Delgado, H. E., Clementini, G., Sarro, L. M., & Garofalo, A. 2018, *MNRAS*, 481, 1195
- Navarrete, C., Belokurov, V., Koposov, S. E., et al. 2017, *MNRAS*, 467, 1329
- Nemec, J. M., Cohen, J. G., Ripepi, V., et al. 2013, *ApJ*, 773, 181
- Peñarrubia, J., Belokurov, V., Evans, N. W., et al. 2010, *MNRAS*, 408, L26
- Peñarrubia, J., Zucker, D. B., Irwin, M. J., et al. 2011, *ApJ*, 727, L2
- Price-Whelan, A. M. 2017, *The Journal of Open Source Software*, 2
- Price-Whelan, A. M., Mateu, C., Iorio, G., et al. 2019, *AJ*, 158, 223
- Reid, M. J., Menten, K. M., Brunthaler, A., et al. 2014, *ApJ*, 783, 130
- Rimoldini, L., Holl, B., Audard, M., et al. 2019, *A&A*, 625, A97
- Romero-Gómez, M., Mateu, C., Aguilar, L., Figueras, F., & Castro-Ginard, A. 2019, *A&A*, 627, A150
- Rybizki, J., Demleitner, M., Fouesneau, M., et al. 2018, *PASP*, 130, 074101
- Schlafly, E. F. & Finkbeiner, D. P. 2011, *ApJ*, 737, 103
- Schlegel, D. J., Finkbeiner, D. P., & Davis, M. 1998, *ApJ*, 500, 525
- Schönrich, R., Binney, J., & Dehnen, W. 2010, *MNRAS*, 403, 1829
- Sesar, B., Hernitschek, N., Dierickx, M. I. P., Fardal, M. A., & Rix, H.-W. 2017a, *ApJ*, 844, L4
- Sesar, B., Hernitschek, N., Mitrović, S., et al. 2017b, *AJ*, 153, 204
- Sesar, B., Vivas, A. K., Duffau, S., & Ivezić, Ž. 2010, *ApJ*, 717, 133
- Shipp, N., Drlica-Wagner, A., Balbinot, E., et al. 2018, *ApJ*, 862, 114
- Totten, E. J. & Irwin, M. J. 1998, *MNRAS*, 294, 1
- Vivas, A. K., Zinn, R., Andrews, P., et al. 2001, *ApJ*, 554, L33
- Vivas, A. K., Zinn, R., & Gallart, C. 2005, *AJ*, 129, 189
- Yang, C., Xue, X.-X., Li, J., et al. 2019, *ApJ*, 886, 154
- Zhang, X., Shi, W. B., Chen, Y. Q., et al. 2017, *A&A*, 597, A54
- Zinn, R. & West, M. J. 1984, *ApJS*, 55, 45

## Appendix A: Reddening to absorption transformations

The reddening maps provided by Schlafly & Finkbeiner (2011) return a value of the colour excess,  $E(B-V)$ , for each pair of celestial coordinates. To obtain the absorption we then assume a proportionality constant,  $R_V$ , of 3.1 (Cardelli et al. 1989). However, this yields the absorption in the V-band,  $A_V$ , so we still need a conversion to the absorption in the G-band,  $A_G$ . For that, we use the empirical relations between the ratio  $\frac{A_G}{A_V}$  and the *Gaia* photometry provided by J.M. Carrasco (priv. comm.) and already used in Romero-Gómez et al. (2019).

## Appendix B: Tailored Gaussian Mixture

Here we explain in more detail the TGM algorithm. We use the particular case of the distance (see Sect. 3.3) to guide the exposition, but the steps are the same for any other quantity that varies as a function of  $\tilde{\Lambda}_\odot$  ( $\mu_{\alpha^*}$  and  $\mu_\delta$ ). We only tweak the parameters to obtain a better performance for each case: bin-size, step-size, threshold, maximum separation and kernel bin-width.

First we take all the stars in the range  $-2.5^\circ \leq \tilde{\Lambda}_\odot < 2.5^\circ$  and obtain a Gaussian kernel to the corresponding distance histogram. Having done that, we evaluate the kernel at 100 000 points and apply a peak finder algorithm (`scipy.signal.find_peaks`) to locate all local maximum. We keep only those whose height are above a certain dimensionless threshold, set arbitrarily so that we can remove the small oscillations appearing on the tails of the distributions due to Poisson noise (0.0075 in this case). The remaining  $n$  peaks are then used as centres of  $n$  normal probability distributions. Finally, we fit the sum of a constant floor level (free parameter) and  $n$  Gaussians for which we set free their widths ( $\sigma$  [kpc]) and amplitudes. For that, we use the Least Square Minimisation algorithm implemented in *Scipy* and find the  $\sigma$  for each component that better reproduce the kernel. In order to avoid spending too much time at each bin, we limit the number of Gaussians to the four with highest height. Three examples of the fitting process are shown in Fig. B.1.

Given that at  $\tilde{\Lambda}_\odot=0^\circ$  the dominant component is that of the Sgr dwarf, we assign the Gaussian with the largest amplitude to the stream. Then, we just repeat this strategy every  $5^\circ$  in both directions, negative and positive  $\tilde{\Lambda}_\odot$ , but now associating to the stream the component most similar to the previous one. To define which is the most similar we apply the following rule: rank the peaks by height, filter out those that are too far apart, and then chose the first one. In this case, we impose a maximum difference between two consecutive peaks of 10 kpc.

This method relies on the separation between the different components at any given  $\tilde{\Lambda}_\odot$ . If they are too close to each other, we need a smaller bin width when creating the kernel to resolve them at the expense of increasing the number of peaks created by simple Poisson noise. On the other hand, if we smooth the kernel too much in an effort to reduce the spurious peaks, the different components can interfere with each other, in which case we would obtain a biased position. Here, we have chosen a value of 0.15 (in the units given by the *Scipy* function) for both the Strip and the nGC3 samples.

In Sect. 3.4 and 3.5, we applied the same procedure but with the following parameters:

- Bin-size:  $2.5^\circ$
- Step-size:  $5^\circ$
- Bin-width: 0.30
- Threshold: 0.10

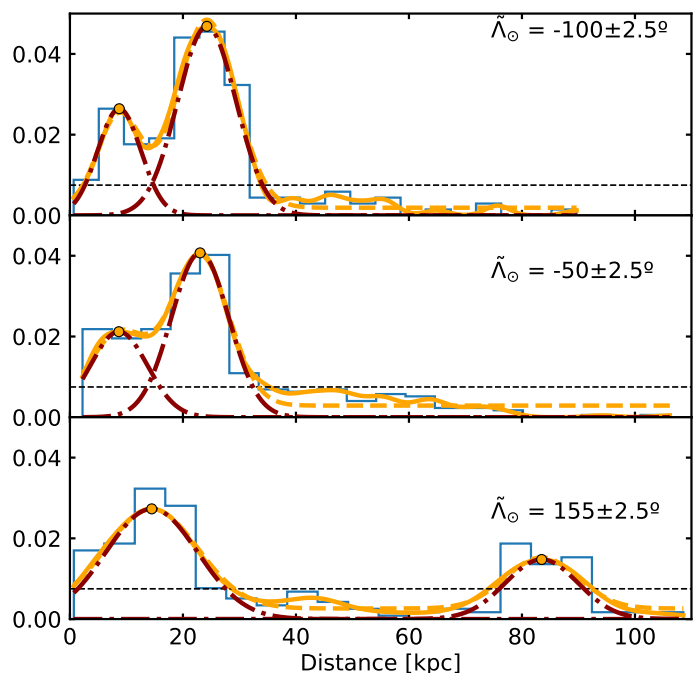


**Fig. B.1.** Example of the TGM applied to the distance distribution at selected bins of  $\tilde{\Lambda}_\odot=[-100^\circ,-50^\circ,155^\circ]$  for the Strip sample. The blue steps show a histogram of the heliocentric distance of all stars with a bin size of  $5^\circ$ . The solid orange line is the kernel obtained with the parameters detailed in the text. The orange dots that appear on top of it are the peaks detected and the red lines the corresponding Gaussian distributions obtained from the fit. Finally, the orange dashed line is the reconstruction of the kernel with the individual Gaussians added together.

- Separation:  $1.5 \text{ mas yr}^{-1}$

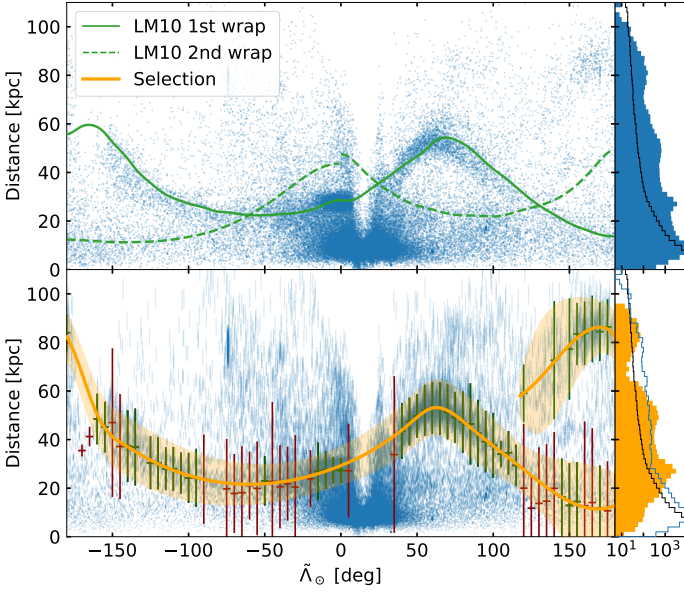
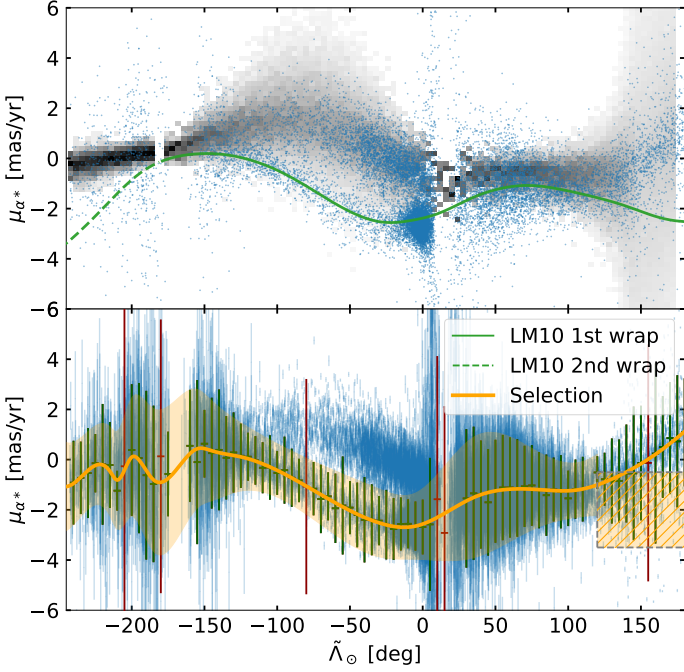
As a final remark, it is also worth mentioning that we tried using the common clustering algorithms like DBSCAN, hierarchical DBSCAN or  $k$ -means. Nevertheless, most of this methods are density-based and, in our case, the Sgr stream presents significant gradients which caused us to obtain sub-optimal results. We acknowledge that there could exist a combination of parameters and a coordinate transformation such that a clean separation between the contamination and the stream stars appears but, after some trial and error, we decided to apply the TGM.

## Appendix C: Strip sample selection process

Here we show the plots of each state of the filtering process starting from a Strip in the sky around the Sgr orbital plane (see Sect. 3.1). First, we apply the TGM to the heliocentric distance (Fig. C.1) then on the proper motion in right ascension (Fig. C.2) and finally, on the proper motion in declination (Fig. C.3). The number of stars remaining after each step can be found in Table 1.

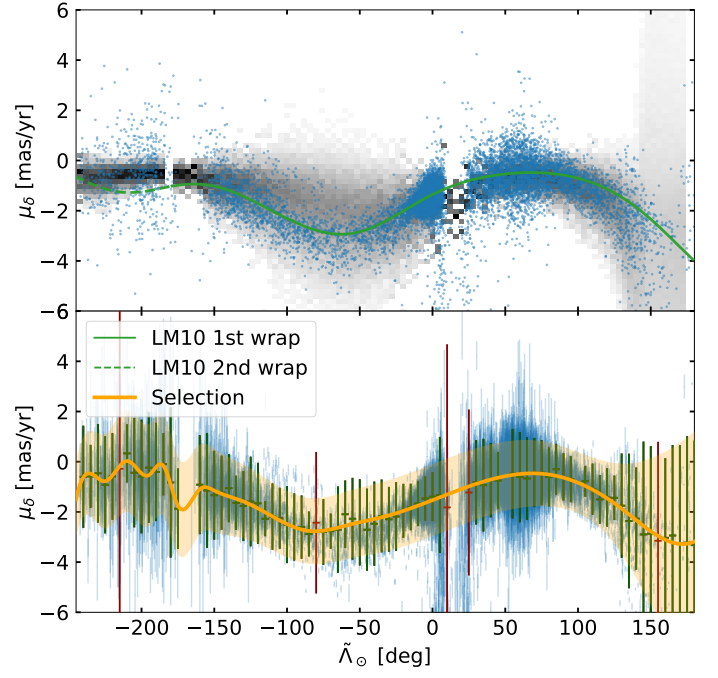
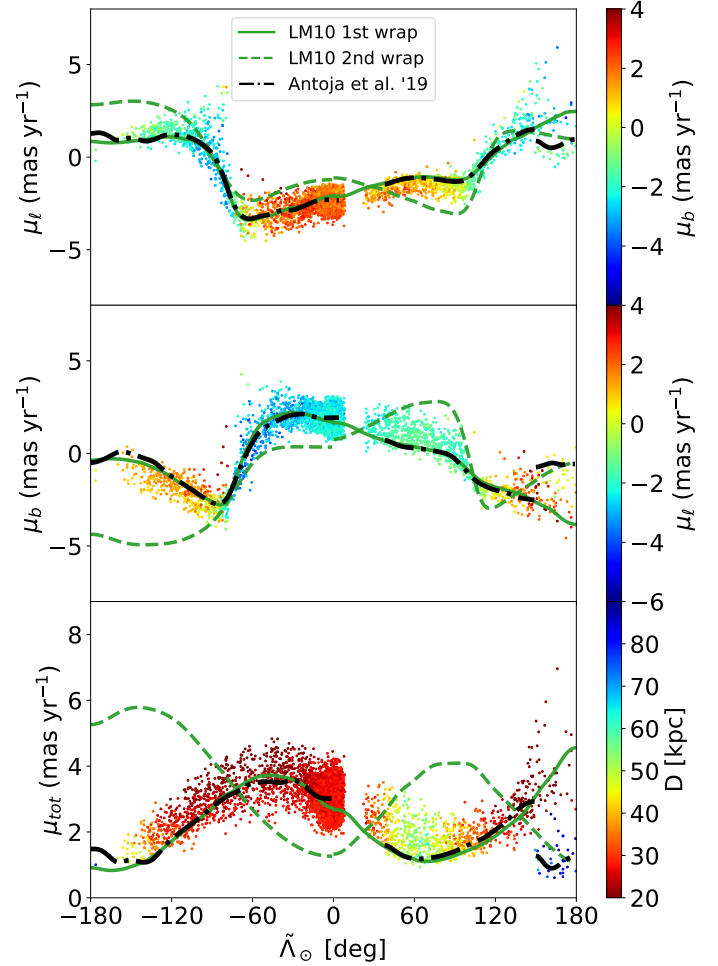
## Appendix D: Summary plots of the nGC3 sample

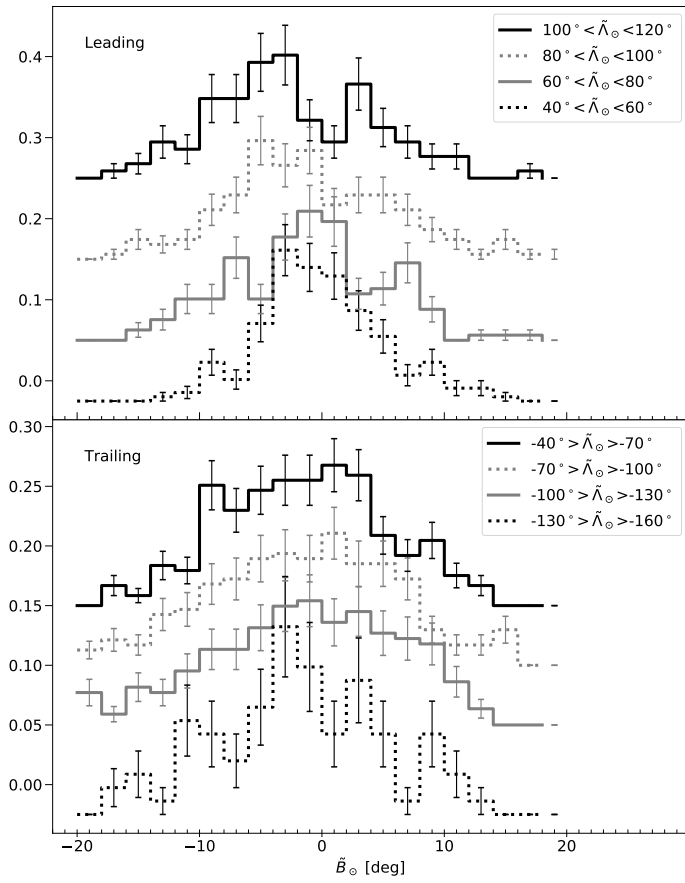
In this Appendix we include the summary plots of the nGC3 sample. In particular, the changes in proper motion in the Galactic reference frame (Fig. D.1) and the detection of the bifurcation (Fig. D.2).


**Fig. C.1.** Same as Fig. 3 for the Strip sample.

**Fig. C.2.** Same as Fig. 4 for the Strip sample.

## Appendix E: Interpolators for median quantities along the stream

We provide a series of interpolators that can be used to obtain the values of the heliocentric distance, proper motion in each reference frame (ICRS, Galactic or Sagittarius) and tangential velocities ( $v_{\tilde{\Lambda}_\odot}$  and  $v_{\tilde{B}_\odot}$ ). The interpolators are given as a table containing the median of the corresponding quantity in bins of  $\tilde{\Lambda}_\odot$  and as a pickled *Python* function (a stream of bytes that represent said object). In the case of the later, we include instructions for loading them into *Python*. All this information, and more, can be found at <https://services.fqa.ub.edu/sagittarius>.


**Fig. C.3.** Same as Fig. 5 for the Strip sample.

**Fig. D.1.** Same as Fig. 6 for the nGC3 sample.



**Fig. D.2.** Same as Fig. 9 for the nGC3 sample.